THE ASTROPHYSICAL JOURNAL, 562:179–207, 2001 November 20

MODELS FOR MULTIBAND INFRARED SURVEYS

CONG XU, CAROL J. LONSDALE, DAVID L. SHUPE, JOANN O'LINGER, AND FRANK MASCI
Infrared Processing and Analysis Center, Jet Propulsion Laboratory, Caltech 100-22, Pasadena, CA 91125
Received 2001 February 4; accepted 2001 July 23

ABSTRACT

Empirical "backward" galaxy evolution models for IR bright galaxies are constrained using multiband IR surveys. A new Monte Carlo algorithm is developed for this task. It exploits a large library of realistic spectral energy distributions (SEDs) of 837 local IR galaxies (*IRAS* 25 μm selected) from the UV (1000 Å) to the radio (20 cm), including *Infrared Space Observatory* (*ISO*) measured 3–13 μm unidentified broad features (UIBs). The basic assumption is that the local correlation between SEDs and mid-infrared (MIR) luminosities can be applied to earlier epochs of the universe, an assumption that will be strongly tested by *SIRTF*. By attaching an SED appropriately drawn from the SED library to every source predicted by a given model, the algorithm enables simultaneous comparisons with multiple surveys in a wide range of wave bands. Three populations of IR sources are considered in the evolution models. These include (1) starburst galaxies, (2) normal late-type galaxies, and (3) galaxies with active galactic nuclei (AGNs). Constrained by data from the literature, our best-fit model ("peak model") predicts that since $z = 1.5$ the population of starburst galaxies undergoes a very strong luminosity evolution [$L = L_0(1+z)^{4.2}$] and also strong density evolution [$\rho = \rho_0(1+z)^2$], the normal late-type galaxy population undergoes a passive luminosity evolution [$L = L_0(1+z)^{1.5}$], and the galaxies with an AGN undergo a pure luminosity evolution similar to that of optical QSOs [$L = L_0(1+z)^{3.5}$]. Prior at $z \geq 1.5$ all evolution rates drop as $(1+z)^{-3}$. The luminosity evolution results in evolution of SEDs of IR bright sources because of the luminosity dependence of the SEDs. Predictions for number counts, confusion limits, redshift distributions, and color-color diagrams are made for multiband surveys using the upcoming *SIRTF* satellite. A Λ cosmology ($\Omega_\Lambda = 0.7$, $\Omega_m = 0.3$, $H_0 = 75$ km s^{-1} Mpc^{-1}) is assumed throughout the paper.

Subject headings: galaxies: luminosity function, mass function — galaxies: Seyfert — galaxies: starburst — infrared: galaxies
On-line material: machine-readable table

1. INTRODUCTION

The first sign of cosmic evolution among infrared (IR) galaxies was detected by Hacking, Condon, & Houck (1987) in the *IRAS* 60 μm deep survey (Hacking & Houck 1987). This was subsequently confirmed by later studies of *IRAS* galaxy populations (Franceschini et al. 1988; Lonsdale & Hacking 1989; Lonsdale et al. 1990; Rowan-Robinson et al. 1990; Saunders et al. 1990; Yahil et al. 1991; Gregorich et al. 1995; Pearson & Rowan-Robinson 1996; Bertin, Dennefeld, & Moshir 1997). Recently, deep mid-IR (MIR) to far-IR (FIR) surveys have been carried out using the *Infrared Space Observatory* (*ISO*) (Kessler et al. 1996). These include ISOCAM surveys at 15, 12, and 6.7 μm (see Elbaz et al. 1998b for a summary of these observations) and ISOPHOT surveys at 90 μm (Oliver et al. 2000; Efstathiou et al. 2000a) and 175 μm (Kawara et al. 1998; Puget et al. 1999; Dole et al. 2001). The results from these surveys (Aussel et al. 1999; Puget et al. 1999; Dole et al. 2001; Clements et al. 1999; Elbaz et al. 1999; Serjeant et al. 2000; Xu 2000, hereafter Paper II) indicate strong cosmic evolution in the population of infrared-emitting galaxies, confirming the earlier results based on smaller samples and less-sophisticated analyses (e.g., Rowan-Robinson et al. 1997; Kawara et al. 1998). This is consistent with the results of SCUBA surveys (Hughes et al. 1998; Barger et al. 1998; Blain et al. 1999) and with the scenario hinted at by the newly discovered cosmic infrared background (CIB) (Puget et al. 1996; Hauser et al. 1998; Dwek et al. 1998; Fixsen et al. 1998), while challenging the results from UV/optical surveys in the sense that substantially more (i.e., a factor of 3–5) star formation in the earlier universe is required to match the IR/submillimeter counts and the CIB (see, e.g., Rowan-Robinson et al. 1997) compared to that derived from the UV/optical surveys (Madau, Pozzetti, & Dickinson 1998; Pozzetti et al. 1998; Steidel et al. 1999). The reason for this discrepancy is attributed to dust extinction, which may hide much of the star formation in the early universe from the UV/optical surveys (see Lonsdale 2000 for a review).

Compared to the UV and optical surveys, the infrared surveys are superior in their insensitivity to dust extinction but are inferior in angular resolution (a few arcseconds compared to the subarcsecond resolution of optical surveys). This not only limits the IR surveys by confusion but also makes the study of the IR morphology of faint IR sources impossible. In order to reveal the true nature of faint IR sources, identifications in other bands, especially in optical and near-IR (NIR) bands where the sources can be resolved easily with current instruments, are usually needed. The multiband studies (including ISOCAM 15 and 6.7 μm surveys) of the Hubble Deep Field (HDF) by Rowan-Robinson et al. (1997) and Aussel et al. (1999) and of the Canada-France Redshift Survey (CFRS) field by Flores et al. (1999) suggest that, compared to their optical counterparts, the ISOCAM sources have significantly redder $(I-K)$ colors (Flores et al. 1999) and are much more likely to be in the interacting/merging systems. On the other hand, such studies are necessarily confined to IR sources that are relatively bright in the optical (e.g., $I \leq 22.5$ mag; Flores et al. 1999), while many IR bright galaxies are optically faint as a result of heavy dust extinction.

IRAS studies showed that galaxies of different nature in the local universe have distinct IR spectral energy distributions (SEDs). Galaxies with bright active galactic nuclei (AGNs) usually have significantly lower $f_{60\,\mu\mathrm{m}}/f_{25\,\mu\mathrm{m}}$ ratios (de Grijp et al. 1985; Fang et al. 1998) than other galaxies. Interacting/starburst galaxies such as M82 have systematically higher $f_{60\,\mu\mathrm{m}}/f_{100\,\mu\mathrm{m}}$ and $f_{25\,\mu\mathrm{m}}/f_{12\,\mu\mathrm{m}}$ ratios than normal galaxies such as the Milky Way (e.g., Helou 1986). In principle, these different characteristics in the IR SEDs for different populations of galaxies should facilitate a tool for identifications of IR galaxies when multiband IR surveys are available, independent of the optical identifications. For *ISO* surveys this may not be very relevant because the ISOPHOT FIR surveys do not match the ISOCAM MIR surveys in depth as a result of severe degradation of the sensitivity of ISOPHOT detectors. However, when the *Space Infrared Telescope Facility* (*SIRTF*) is launched in mid-2002, simultaneous deep surveys in seven MIR to FIR bands (3.6, 4.5, 5.8, 8.0, 24, 70, and 160 μm) will be possible (Bicay et al. 1999). These will include the Guaranteed Time Observer programs with MIPS and IRAC,[1] the large-area Legacy survey SWIRE,[2] and the very deep Legacy survey GOODS.[3]

Significant K-corrections will occur in the observed SEDs of faint sources in deep IR surveys. In particular, in the rest-frame wavelength range between 3 and 20 μm there are several broadband features (see Puget & Léger 1989 for a review), often referred to as the unidentified infrared bands (UIBs), which are ubiquitously present in the MIR spectra of local galaxies with equivalent widths up to several microns (Helou et al. 2000), with the exception of type 1 Seyfert galaxies (Clavel et al. 2000). If these features are also present in the SEDs of high-redshift galaxies, substantial K-corrections will occur when any of the features redshift in or out of the bandpass of an IR filter. These effects may indeed be beneficial rather than annoying, for they may facilitate IR photometric redshift techniques.

Xu et al. (1998, hereafter Paper I) studied the effect of K-corrections due to UIBs on number counts of MIR surveys. In that work, a three-component model, with empirically determined MIR SED templates of (1) a cirrus/PDR component, (2) a starburst component, and (3) an AGN component, is developed for infrared (3–120 μm) SEDs of galaxies. The model is then applied to a complete *IRAS* 25 μm selected sample of 1406 local galaxies ($z \leq 0.1$; Shupe et al. 1998). Results based on these 1406 spectra show that the MIR emission features cause significant effects on the redshift dependence of the K-corrections, which in turn affect deep counts and redshift distributions in MIR surveys. In Paper II we found that indeed the sharp peak at about 0.4 mJy in the Euclidean normalized differential counts at 15 μm (Elbaz et al. 1999) can be explained by the effects of UIBs, together with an evolution rate significantly stronger than derived in previous *IRAS* studies, eliminating the need for a hypothetical "new population" (Elbaz et al. 1998a).

In this paper we expand the models in Paper I in several aspects.

[1] http://sirtf.caltech.edu/ROC/Titles_abstracts.html.
[2] http://www.ipac.caltech.edu/SWIRE.
[3] http://www.stsci.edu/science/goods.

1. First of all, the analytical algorithm of the number count model, which includes a proper treatment of the K-correction (eqs. [23], [24], and [25] in Paper I), is replaced by a Monte Carlo algorithm, in which every source (galaxy) in a volume of given redshift and in a given luminosity bin is assigned an SED appropriately selected from the SED library (837 SEDs). The source's flux densities in different bands are then calculated by convolving the redshifted SED with the bandpasses of filters. In this way, we effectively simulate a virtual sky for a given evolution model. This not only enables the simultaneous comparisons with counts in different bands but also preserves the correlations between flux densities of different bands. The latter feature allows us to predict color-color diagrams of different populations as a function of redshift, facilitating the exploration of photometric redshift indicators.

2. In the "backward evolution" model, instead of treating all IR sources as a single population, in this work they are separated into three populations, in a similar spirit as in the model of Franceschini et al. (1988; see also Roche & Eales 1999): (1) normal late-type galaxies, (2) interacting/starburst galaxies, and (3) galaxies with AGNs. These different populations are assumed to have different cosmic evolution rates.

3. The wavelength coverage of our SED library is expanded from 3–120 μm to 1000 Å to 20 cm. This is done by collecting from the literature the optical/NIR (B, J, H, and K_s bands) magnitudes and the radio continuum (20 cm) flux densities for galaxies in our SED sample and by extrapolating from *IRAS* 60 and 100 μm bands to submillimeter bands using empirically determined correlations.

The goal of this paper is to provide a set of comprehensive "backward evolution" models (a category of galaxy evolution models in which number densities and other properties, e.g., luminosities in different bands, of local galaxies are evolved "backward" in time from the present, i.e., with increasing redshift, according to some parametric prescriptions; see Lonsdale 2000 for a review) for future multiband surveys, in particular those to be conducted with *SIRTF*. The model parameters will be constrained by observations available in the literature. This includes not only the *ISO* deep surveys but also the optical/NIR surveys, SCUBA surveys, and radio deep surveys because our SEDs now cover all of these wave bands. Constraints derived from the CIB will also be incorporated. The strength of models being constrained by such a wide range of data has already been demonstrated in several previous papers (e.g., Blain et al. 1999; Trentham, Blain, & Goldader 1999; Adelberger & Steidel 2000; Rowan-Robinson 2001, hereafter R01).

The model focuses on IR bright galaxies and therefore is not expected to match observed number counts in any band for which there is a substantial contribution from IR quiet populations, e.g., the K band, because E/S0 populations are missing from our model, and the bright radio counts, which are dominated by radio galaxies.

Throughout the paper the cosmology model specified by the following parameters is adopted: $H_0 = 75$ km s^{-1} Mpc^{-1}, $\Omega_m = 0.3$, $\Omega_\Lambda = 0.7$.

2. SED LIBRARY

As in Paper I, our SED sample is drawn from the *IRAS* 25 μm selected sample (complete down to $f_{25\mu} = 0.25$ Jy) by

Shupe et al. (1998) and contains 1455 galaxies, 1406 of them with redshifts ≤ 0.1. As pointed out by Spinoglio et al. (1995), the MIR luminosities correlate well with the bolometric luminosities. Therefore, MIR-selected samples, such as ours, have fair representations of different populations of IR sources. However, E/S0 galaxies, which are $\sim 20\%$ in optically selected galaxy samples but mostly undetected by *IRAS*, are not included in our SED sample.

In Paper I, a three-component (cirrus/photodissociation region [PDR], starburst, and AGN) MIR SED model is applied to these galaxies, predicting an SED from 3 to 120 μm for each of them. In order to expand the SEDs to the optical and NIR bands, i.e., B (4400 Å), J (1.2 μm), H (1.6 μm), and K_s (2.2 μm), we searched the literature. B magnitudes of 1339 galaxies were found in the NASA/IPAC Extragalactic Database (NED). The NIR magnitudes are taken mainly from the 2MASS Second Incremental Data Release via the IRSA facility[4] where J, H, and K_s magnitudes of 790 galaxies were found. In addition, NIR magnitudes of 413 galaxies in our sample are given in Spinoglio et al. (1995), 244 of which are overlapped with the 2MASS matches. Whenever NIR magnitudes are available from both 2MASS and Spinoglio et al. (1995), 2MASS data take precedence. Altogether, J, H, and K_s magnitudes are found for 959 galaxies in our sample. The radio continuum flux densities at 20 cm, $S_{1.4\,\mathrm{GHz}}$, were searched for in both the NVSS (Condon et al. 1998) and FIRST (Becker, White, & Helfand 1995) catalogs of NRAO. Among 1406 galaxies in our sample, 1170 are found in one of these two surveys (the rest are in the sky area not visible by VLA). It is found that 854 galaxies in our sample have B, J, H, and K_s magnitudes and radio continuum flux at 1.4 GHz. After excluding 17 galaxies that were undetected by *IRAS* in both the 60 and 100 μm bands (whose IR SEDs are highly uncertain), we select a final SED sample of 837 galaxies. Note that the 569 galaxies in the original sample (1406 galaxies) that do not make it into the final SED sample are mostly galaxies without NIR magnitudes. This is mainly due to the fact that data for NIR sources in a large fraction of the sky have not been released by the 2MASS survey (the major source of the NIR data) yet. Since both the 2MASS survey and the VLA surveys are much deeper than the *IRAS* survey, the NIR magnitudes or the 20 cm flux density are missing for a source in the 25 μm selected sample only when the sky region is missing in the corresponding database. Therefore, no bias is introduced into the final SED sample when sources without NIR or radio fluxes are excluded.

For each galaxy in the SED sample, the broadband UV–optical–NIR (1000 Å to 4 μm) SED is estimated by a spline fit of the fluxes in B, J, H, and K_s bands, altogether with the predicted 4 μm flux density from the MIR SED model (Paper I). It should be noted that at the UV wavelengths (1000–4000 Å) the predicted fluxes are extrapolations from the available data, and caution should be applied when these predictions are used. This aspect of the model will be improved in the next paper, using the new UV data that are just now becoming available for ultraluminous infrared galaxies (ULIRGs) and other IR bright galaxies.

The MIR (4–16 μm) SED is determined using the MIR SED model developed in Paper I, including a full treatment of the UIB features (absent in type 1 AGNs). Then the SED in the wavelength range 16–1200 μm is specified by a spline fit of *IRAS* data at 25, 60, and 100 μm, together with the 16 μm flux density predicted by the MIR SED model, and the 170, 240, 450, 850, and 1200 μm flux densities predicted by empirical correlations between the given submillimeter band flux and the *IRAS* 60 and 100 μm fluxes that are derived from available submillimeter data collected from the literature (Appendix).

The radio continuum flux density at 20 cm ($S_{1.4\,\mathrm{GHz}}$) is extrapolated to 6.2 cm ($S_{4.8\,\mathrm{GHz}}$) and 2.8 cm ($S_{10.2\,\mathrm{GHz}}$) using the mean spectral indices $\alpha_{20\mathrm{cm}/6.2\mathrm{cm}} = 0.79$ and $\alpha_{6.2\mathrm{cm}/2.8\mathrm{cm}} = 0.70$, found for Shapley-Ames galaxies (Niklas, Klein, & Wielebinski 1997). These radio flux densities are then linked to the end of the IR/submillimeter SED at 1200 μm by spline fit.

In Figure 1 we show the SEDs that are binned according to population (see the next section) and the 25 μm luminosity (Table 1). For each bin, the mean SED and its 1 σ dispersion are also plotted in the corresponding panel in Figure 1, and the values are listed in Table 2.

As examples, in Figure 2 observational data of 12 well-known galaxies are compared with model SEDs. The data are collected from the literature, and the sources are (1) broadband optical magnitudes (NED), (2) NIR magnitudes (2MASS; Spinoglio et al. 1995), (3) FIR/submillimeter flux densities (*IRAS*; Benford 1999; Dunne et al. 2000; Rigopoulou, Lawrence, & Rowan-Robinson 1996; Lisenfeld, Isaak, & Hills 2000; Carico et al. 1992; Chini, Kruegel, & Kreysa 1986; Andreani & Franceschini 1996; Roche & Chandler 1993), and (4) radio continuum flux densities (Niklas et al. 1995; Condon et al. 1990). The agreements between the data and the model SEDs are remarkably good in general.

TABLE 1

BINS OF SED LIBRARY

Population	$L_{25\,\mu\mathrm{m}}$ Bin[a]		Number of Sources
	log L_1	log L_2	
Normals	6	8	3
	8	9	81
	9	9.4	65
	9.4	9.8	63
	9.8	10.2	36
	10.2	11	18
Starbursts......	6	8	2
	8	9	31
	9	9.4	46
	9.4	9.8	85
	9.8	10.2	80
	10.2	10.6	78
	10.6	11	41
	11	12	16
AGNs	6	10	63
	10	12	129

[a] $L_{25\mu\mathrm{m}} = \nu L_\nu(25\ \mu\mathrm{m})$, in units of $L_\odot$. Luminosity bins are defined by $\log L_1 < \log L_{25\mu\mathrm{m}} \leq \log L_2$.

[4] The NASA/IPAC Infrared Science Archive (IRSA) is a NASA project focused on providing software and Internet services to facilitate astronomical discoveries, to support the production of new astronomical data products, and to plan future observations utilizing the data archives from infrared astrophysics missions supported at the Infrared Processing and Analysis Center (IPAC).

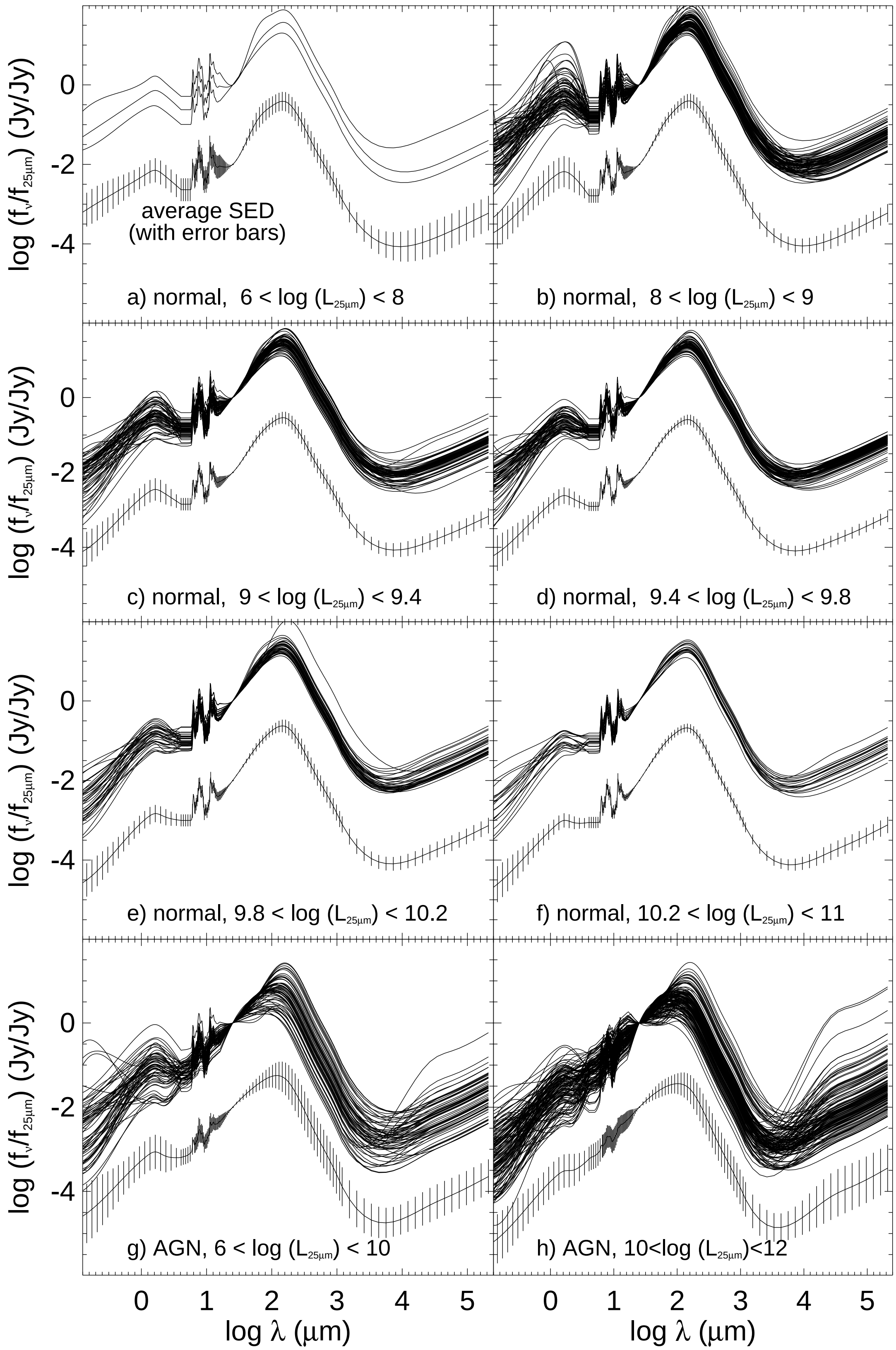

FIG. 1.—SEDs in different population and $L_{25\,\mu\mathrm{m}}$ bins. Panels (*a*)–(*f*) are for "normals," panels (*g*) and (*h*) are for "AGNs," and panels (*i*)–(*p*) are for "starbursts." Mean SEDs are plotted with 1 σ dispersions (*vertical bars*).

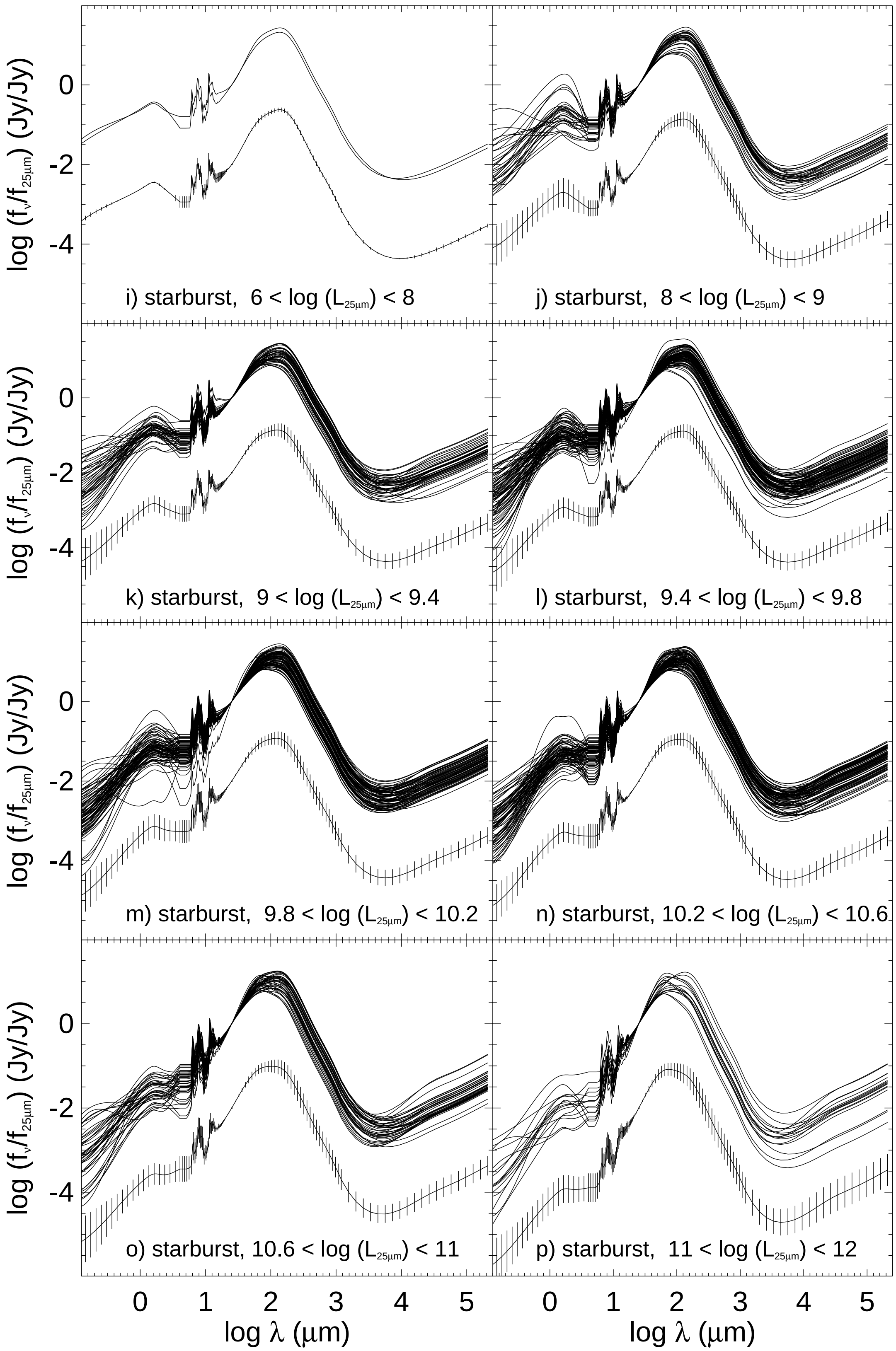

FIG. 1.—*Continued*

TABLE 2

AVERAGE SEDs [log ($f_\nu/f_{25\mu m}$)] OF IR SOURCES IN log $L_{25\mu m}$ BINS

log λ (μm)	Normal Late-Type Galaxies log ($L_{25\mu m}/L_\odot$) Bins: 7±1	8.5±0.5	9.2±0.2	9.6±0.2	10.0±0.2	10.6±0.4	AGNs log ($L_{25\mu m}/L_\odot$) Bins: 8±2	11±1
−1.00	−1.31±0.35	−1.78±0.57	−2.20±0.48	−2.31±0.52	−2.65±0.42	−2.80±0.45	−2.68±0.67	−3.30±0.57
−0.76	−1.05±0.44	−1.57±0.44	−1.94±0.44	−2.05±0.45	−2.39±0.41	−2.49±0.44	−2.42±0.69	−3.02±0.57
−0.51	−0.82±0.41	−1.21±0.37	−1.56±0.36	−1.68±0.34	−1.99±0.33	−2.11±0.35	−2.07±0.55	−2.63±0.48
−0.27	−0.58±0.33	−0.80±0.35	−1.12±0.29	−1.27±0.24	−1.54±0.25	−1.69±0.25	−1.68±0.40	−2.21±0.40
−0.03	−0.35±0.28	−0.42±0.39	−0.72±0.30	−0.88±0.22	−1.11±0.22	−1.29±0.20	−1.31±0.38	−1.81±0.39
0.21	−0.15±0.31	−0.18±0.39	−0.45±0.30	−0.62±0.22	−0.83±0.22	−1.00±0.18	−1.06±0.41	−1.52±0.40
0.46	−0.42±0.29	−0.47±0.31	−0.67±0.23	−0.79±0.18	−0.96±0.18	−1.08±0.14	−1.19±0.31	−1.42±0.34
0.64	−0.64±0.29	−0.79±0.18	−0.85±0.17	−0.91±0.12	−1.00±0.15	−1.06±0.14	−1.18±0.19	−1.19±0.30
0.83	−0.27±0.29	−0.43±0.18	−0.49±0.17	−0.57±0.13	−0.69±0.15	−0.75±0.14	−0.89±0.19	−0.93±0.27
0.87	0.16±0.28	−0.02±0.18	−0.10±0.17	−0.19±0.13	−0.37±0.18	−0.54±0.15	−0.69±0.25	−0.83±0.25
0.91	0.05±0.29	−0.10±0.18	−0.16±0.16	−0.22±0.12	−0.28±0.14	−0.25±0.14	−0.64±0.21	−0.70±0.26
0.95	−0.35±0.30	−0.46±0.17	−0.49±0.16	−0.51±0.11	−0.54±0.14	−0.49±0.14	−0.77±0.17	−0.73±0.26
0.99	−0.43±0.29	−0.59±0.17	−0.65±0.16	−0.69±0.11	−0.74±0.13	−0.74±0.12	−0.80±0.18	−0.78±0.26
1.04	−0.21±0.28	−0.39±0.18	−0.47±0.16	−0.54±0.12	−0.62±0.13	−0.63±0.12	−0.65±0.17	−0.66±0.25
1.08	0.15±0.29	0.00±0.17	−0.06±0.16	−0.12±0.11	−0.19±0.14	−0.17±0.13	−0.43±0.17	−0.48±0.24
1.12	0.07±0.29	−0.07±0.17	−0.11±0.15	−0.15±0.11	−0.19±0.13	−0.18±0.11	−0.39±0.15	−0.40±0.22
1.16	−0.07±0.29	−0.21±0.16	−0.26±0.14	−0.32±0.10	−0.39±0.12	−0.42±0.08	−0.39±0.14	−0.37±0.21
1.20	−0.04±0.29	−0.19±0.16	−0.24±0.14	−0.30±0.10	−0.37±0.11	−0.40±0.07	−0.35±0.14	−0.31±0.21
1.25	−0.06±0.21	−0.17±0.12	−0.20±0.11	−0.25±0.08	−0.31±0.09	−0.34±0.06	−0.27±0.11	−0.25±0.18
1.29	−0.07±0.14	−0.14±0.08	−0.16±0.07	−0.19±0.05	−0.23±0.06	−0.25±0.04	−0.20±0.08	−0.18±0.13
1.34	−0.06±0.06	−0.08±0.04	−0.09±0.03	−0.11±0.02	−0.13±0.02	−0.14±0.02	−0.10±0.04	−0.09±0.06
1.40	0.00±0.00	0.00±0.00	0.00±0.00	0.00±0.00	0.00±0.00	0.00±0.00	0.00±0.00	0.00±0.00
1.51	0.25±0.02	0.24±0.03	0.24±0.03	0.24±0.03	0.25±0.02	0.26±0.02	0.18±0.05	0.16±0.08
1.66	0.75±0.15	0.67±0.08	0.63±0.08	0.62±0.06	0.61±0.07	0.63±0.07	0.39±0.12	0.34±0.15
1.81	1.19±0.26	1.07±0.13	1.00±0.12	0.97±0.08	0.94±0.11	0.94±0.10	0.57±0.18	0.48±0.20
1.96	1.42±0.24	1.37±0.14	1.27±0.12	1.23±0.09	1.20±0.11	1.18±0.10	0.71±0.24	0.55±0.23
2.11	1.57±0.23	1.56±0.17	1.44±0.15	1.39±0.12	1.36±0.15	1.31±0.10	0.75±0.33	0.53±0.30
2.26	1.53±0.25	1.55±0.20	1.41±0.18	1.35±0.15	1.31±0.18	1.25±0.12	0.59±0.41	0.32±0.37
2.41	1.21±0.25	1.26±0.22	1.10±0.19	1.04±0.17	1.00±0.20	0.92±0.12	0.22±0.46	−0.08±0.41
2.55	0.75±0.25	0.80±0.22	0.64±0.20	0.58±0.17	0.54±0.20	0.46±0.12	−0.25±0.46	−0.55±0.41
2.70	0.29±0.25	0.33±0.22	0.17±0.19	0.12±0.17	0.07±0.20	0.00±0.12	−0.71±0.46	−1.01±0.41
2.85	−0.14±0.25	−0.09±0.22	−0.25±0.19	−0.31±0.17	−0.35±0.20	−0.43±0.12	−1.14±0.46	−1.44±0.41
2.99	−0.59±0.25	−0.54±0.22	−0.70±0.20	−0.76±0.17	−0.80±0.20	−0.88±0.12	−1.59±0.46	−1.89±0.41
3.19	−1.20±0.25	−1.16±0.21	−1.31±0.19	−1.37±0.17	−1.41±0.20	−1.48±0.12	−2.19±0.45	−2.47±0.40
3.53	−1.83±0.29	−1.79±0.19	−1.90±0.18	−1.94±0.15	−1.97±0.18	−2.02±0.13	−2.68±0.39	−2.86±0.34
3.86	−2.06±0.35	−2.04±0.18	−2.07±0.19	−2.10±0.14	−2.09±0.17	−2.12±0.15	−2.72±0.35	−2.73±0.37
4.20	−2.02±0.41	−2.01±0.21	−1.98±0.21	−1.99±0.15	−1.96±0.19	−1.96±0.19	−2.51±0.38	−2.37±0.49
4.54	−1.83±0.44	−1.82±0.23	−1.77±0.22	−1.77±0.16	−1.73±0.20	−1.71±0.21	−2.24±0.41	−2.03±0.56
4.87	−1.58±0.43	−1.58±0.23	−1.53±0.22	−1.53±0.16	−1.49±0.20	−1.48±0.21	−2.01±0.41	−1.81±0.55
5.21	−1.32±0.43	−1.31±0.23	−1.26±0.22	−1.26±0.16	−1.23±0.20	−1.21±0.21	−1.74±0.41	−1.54±0.55

log λ (μm)	Starburst Galaxies log ($L_{25\mu m}/L_\odot$) Bins: 7±1	8.5±0.5	9.2±0.2	9.6±0.2	10.0±0.2	10.4±0.2	10.8±0.2	11.5±0.5
−1.00	−1.54±0.04	−2.16±0.51	−2.45±0.56	−2.73±0.57	−2.95±0.46	−3.20±0.45	−3.25±0.51	−3.81±0.61
−0.76	−1.26±0.06	−1.95±0.49	−2.20±0.53	−2.48±0.56	−2.69±0.47	−2.95±0.46	−3.01±0.54	−3.53±0.53
−0.51	−1.04±0.04	−1.63±0.39	−1.84±0.41	−2.08±0.42	−2.29±0.36	−2.52±0.36	−2.64±0.42	−3.12±0.40
−0.27	−0.85±0.01	−1.26±0.30	−1.44±0.27	−1.62±0.27	−1.84±0.26	−2.03±0.26	−2.22±0.28	−2.66±0.32
−0.03	−0.65±0.01	−0.91±0.32	−1.07±0.21	−1.19±0.24	−1.41±0.29	−1.57±0.25	−1.83±0.25	−2.23±0.34
0.21	−0.45±0.02	−0.70±0.36	−0.82±0.22	−0.93±0.27	−1.14±0.31	−1.28±0.25	−1.56±0.26	−1.92±0.33
0.46	−0.73±0.02	−0.93±0.29	−1.00±0.19	−1.08±0.23	−1.25±0.26	−1.37±0.23	−1.56±0.23	−1.93±0.30
0.64	−0.94±0.15	−1.10±0.20	−1.10±0.21	−1.17±0.26	−1.27±0.29	−1.38±0.31	−1.45±0.30	−1.89±0.34
0.83	−0.57±0.14	−0.73±0.19	−0.74±0.20	−0.82±0.23	−0.93±0.26	−1.03±0.27	−1.02±0.30	−1.31±0.37
0.87	−0.14±0.15	−0.32±0.19	−0.34±0.20	−0.45±0.23	−0.60±0.27	−0.80±0.27	−0.90±0.25	−1.31±0.27
0.91	−0.25±0.14	−0.41±0.19	−0.41±0.20	−0.47±0.23	−0.53±0.26	−0.55±0.27	−0.53±0.30	−0.89±0.31
0.95	−0.64±0.13	−0.74±0.16	−0.71±0.17	−0.74±0.20	−0.77±0.22	−0.76±0.24	−0.72±0.28	−1.06±0.30
0.99	−0.73±0.14	−0.87±0.16	−0.87±0.17	−0.91±0.19	−0.94±0.20	−0.97±0.18	−1.04±0.17	−1.31±0.21
1.04	−0.50±0.14	−0.65±0.13	−0.67±0.15	−0.73±0.15	−0.78±0.17	−0.84±0.15	−0.92±0.14	−1.19±0.15
1.08	−0.14±0.14	−0.27±0.14	−0.27±0.16	−0.32±0.17	−0.38±0.19	−0.40±0.20	−0.36±0.24	−0.72±0.25
1.12	−0.22±0.13	−0.32±0.12	−0.31±0.14	−0.33±0.15	−0.35±0.16	−0.35±0.13	−0.37±0.12	−0.56±0.15
1.16	−0.35±0.12	−0.42±0.07	−0.42±0.10	−0.44±0.09	−0.47±0.09	−0.48±0.05	−0.49±0.05	−0.57±0.12

TABLE 2—*Continued*

log λ (μm)	Starburst Galaxies log $(L_{25\mu m}/L_{\odot})$ Bins							
	7 ± 1	8.5 ± 0.5	9.2 ± 0.2	9.6 ± 0.2	10.0 ± 0.2	10.6 ± 0.4	8 ± 2	11 ± 1
1.20......	-0.32 ± 0.11	-0.39 ± 0.07	-0.39 ± 0.10	-0.41 ± 0.08	-0.43 ± 0.08	-0.41 ± 0.04	-0.43 ± 0.06	-0.47 ± 0.11
1.25......	-0.26 ± 0.08	-0.32 ± 0.05	-0.32 ± 0.07	-0.33 ± 0.06	-0.36 ± 0.06	-0.37 ± 0.03	-0.38 ± 0.03	-0.41 ± 0.09
1.29......	-0.21 ± 0.06	-0.24 ± 0.03	-0.24 ± 0.05	-0.25 ± 0.04	-0.26 ± 0.04	-0.27 ± 0.02	-0.28 ± 0.02	-0.31 ± 0.06
1.34......	-0.12 ± 0.02	-0.13 ± 0.01	-0.13 ± 0.02	-0.14 ± 0.02	-0.14 ± 0.02	-0.15 ± 0.01	-0.15 ± 0.01	-0.16 ± 0.03
1.40......	0.00 ± 0.00	0.00 ± 0.00	0.00 ± 0.00	0.00 ± 0.00	0.00 ± 0.00	0.00 ± 0.00	0.00 ± 0.00	0.00 ± 0.00
1.51......	0.29 ± 0.01	0.27 ± 0.02	0.28 ± 0.02	0.28 ± 0.02	0.28 ± 0.03	0.29 ± 0.04	0.29 ± 0.03	0.31 ± 0.05
1.66......	0.74 ± 0.03	0.66 ± 0.07	0.67 ± 0.07	0.66 ± 0.08	0.65 ± 0.08	0.68 ± 0.10	0.67 ± 0.08	0.70 ± 0.11
1.81......	1.10 ± 0.06	0.95 ± 0.12	0.96 ± 0.11	0.94 ± 0.12	0.92 ± 0.12	0.94 ± 0.13	0.91 ± 0.11	0.90 ± 0.15
1.96......	1.28 ± 0.06	1.09 ± 0.15	1.10 ± 0.13	1.07 ± 0.15	1.04 ± 0.14	1.04 ± 0.14	0.99 ± 0.13	0.90 ± 0.17
2.11......	1.38 ± 0.05	1.14 ± 0.19	1.14 ± 0.17	1.11 ± 0.19	1.07 ± 0.17	1.05 ± 0.17	0.97 ± 0.17	0.81 ± 0.22
2.26......	1.29 ± 0.06	1.01 ± 0.22	1.01 ± 0.21	0.98 ± 0.23	0.93 ± 0.21	0.89 ± 0.21	0.80 ± 0.22	0.58 ± 0.28
2.41......	0.95 ± 0.06	0.65 ± 0.24	0.65 ± 0.23	0.61 ± 0.25	0.56 ± 0.23	0.51 ± 0.23	0.41 ± 0.24	0.15 ± 0.31
2.55......	0.48 ± 0.06	0.19 ± 0.24	0.18 ± 0.24	0.15 ± 0.25	0.10 ± 0.23	0.04 ± 0.23	-0.06 ± 0.25	-0.32 ± 0.31
2.70......	0.02 ± 0.06	-0.27 ± 0.24	-0.28 ± 0.23	-0.32 ± 0.25	-0.37 ± 0.23	-0.42 ± 0.23	-0.52 ± 0.25	-0.78 ± 0.31
2.85......	-0.40 ± 0.06	-0.70 ± 0.24	-0.70 ± 0.23	-0.74 ± 0.25	-0.79 ± 0.23	-0.85 ± 0.23	-0.95 ± 0.25	-1.20 ± 0.31
2.99......	-0.86 ± 0.06	-1.15 ± 0.24	-1.16 ± 0.24	-1.19 ± 0.25	-1.24 ± 0.23	-1.30 ± 0.23	-1.40 ± 0.25	-1.66 ± 0.31
3.19......	-1.47 ± 0.05	-1.76 ± 0.24	-1.76 ± 0.23	-1.79 ± 0.25	-1.84 ± 0.23	-1.90 ± 0.23	-2.00 ± 0.24	-2.25 ± 0.31
3.53......	-2.11 ± 0.03	-2.29 ± 0.22	-2.28 ± 0.21	-2.30 ± 0.23	-2.35 ± 0.21	-2.40 ± 0.22	-2.47 ± 0.22	-2.69 ± 0.31
3.86......	-2.35 ± 0.00	-2.39 ± 0.20	-2.36 ± 0.21	-2.37 ± 0.23	-2.42 ± 0.20	-2.45 ± 0.22	-2.48 ± 0.21	-2.65 ± 0.33
4.20......	-2.32 ± 0.04	-2.22 ± 0.21	-2.18 ± 0.23	-2.18 ± 0.24	-2.22 ± 0.20	-2.25 ± 0.24	-2.24 ± 0.22	-2.36 ± 0.36
4.54......	-2.14 ± 0.05	-1.98 ± 0.22	-1.93 ± 0.24	-1.92 ± 0.25	-1.96 ± 0.21	-1.99 ± 0.25	-1.96 ± 0.23	-2.06 ± 0.38
4.87......	-1.89 ± 0.05	-1.74 ± 0.22	-1.69 ± 0.24	-1.68 ± 0.25	-1.73 ± 0.21	-1.75 ± 0.24	-1.73 ± 0.23	-1.83 ± 0.37
5.21......	-1.62 ± 0.05	-1.48 ± 0.22	-1.42 ± 0.24	-1.42 ± 0.25	-1.46 ± 0.21	-1.48 ± 0.24	-1.46 ± 0.23	-1.56 ± 0.37

NOTE.—1 σ dispersions are also given. Table 2 is also available in machine-readable form in the electronic edition of the *Astrophysical Journal.*

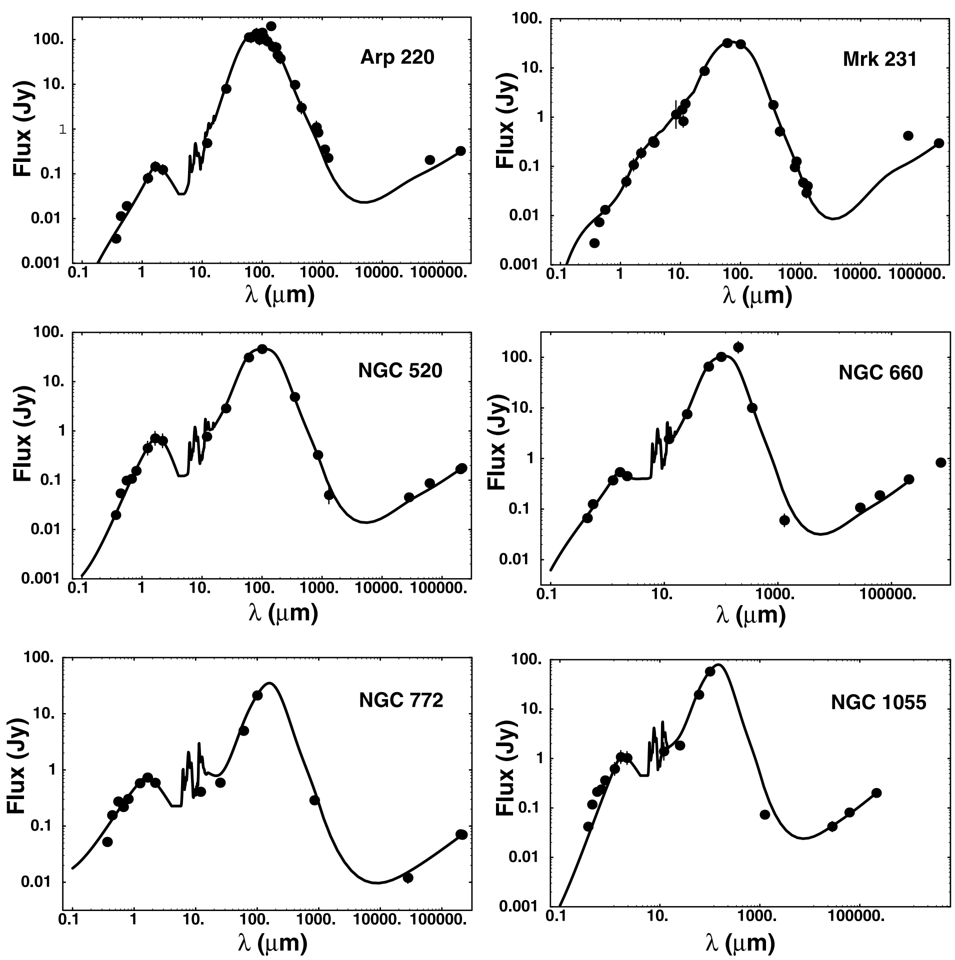

FIG. 2.—Comparisons between model SEDs (*curves*) and observational data (*filled circles with error bars*) for 12 galaxies

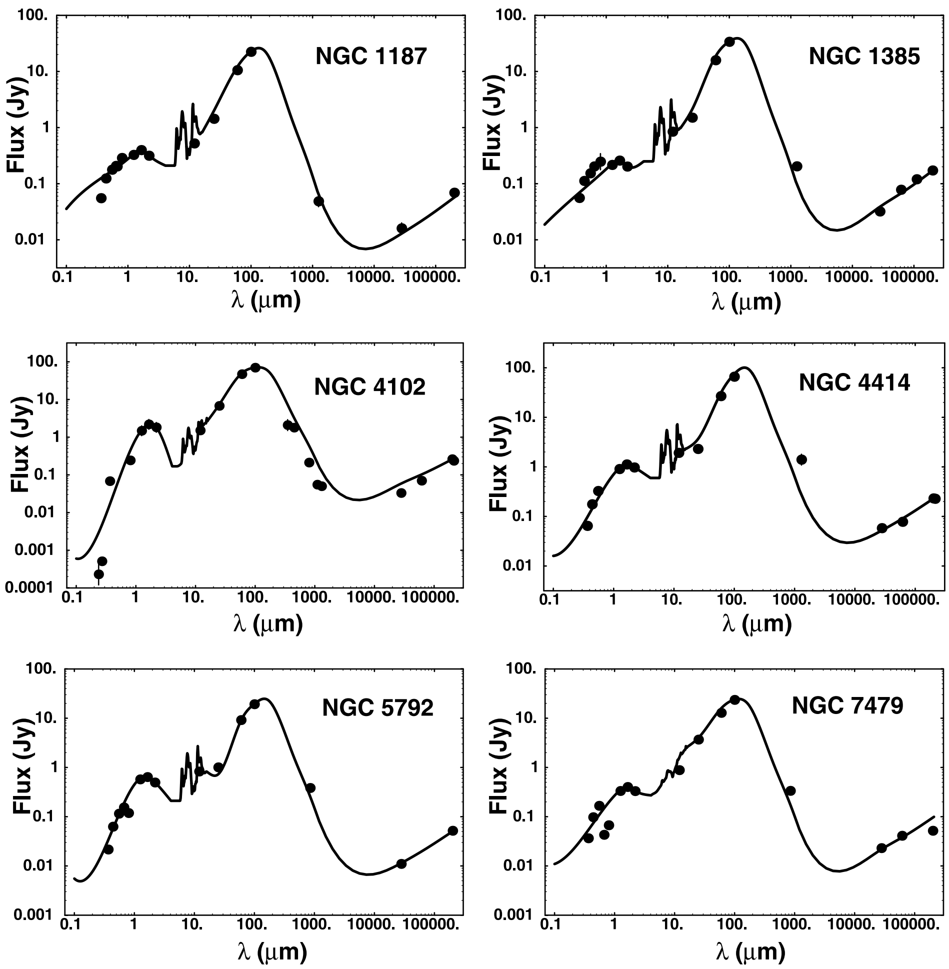

FIG. 2.—*Continued*

3. "BACKWARD EVOLUTION" MODELS FOR MULTIBAND SURVEYS

3.1. *Three Populations of IR-emitting Galaxies and Their LLFs*

In Papers I and II, it is assumed that all IR sources evolve as a single population. Here we improve on that formulation by adopting a model in which IR sources can be separated into three populations, in a similar spirit as in the model of Franceschini et al. (1988; see also Roche & Eales 1999): (1) normal late-type galaxies, (2) interacting/starburst galaxies, and (3) galaxies with AGNs.

To enable these different galaxy populations to evolve at different rates, the model requires a local luminosity function (LLF) for each component. We began with the 25 μm flux density–limited sample of 1455 galaxies of Shupe et al. (1998). Although classifications of many of the galaxies as AGNs, normal galaxies, etc., are available in databases such as NED, to treat the sample in a more uniform way, we use IR color–based criteria to divide our sample into different populations (for a discussion see Paper I; Fang et al. 1998). We chose the following *IRAS* color boundaries:

1. "AGNs": $f_{60\mu m}/f_{25\mu m} \le 5$.
2. "Starbursts": $f_{60\mu m}/f_{25\mu m} > 5$ and $f_{100\mu m}/f_{60\mu m} < 2$.
3. "Normals": $f_{60\mu m}/f_{25\mu m} > 5$ and $f_{100\mu m}/f_{60\mu m} \ge 2$.

This division results in 356 galaxies classified as "AGNs," 456 galaxies as "normal," and 643 galaxies as "starbursts." We note that our color selection method for AGNs will not be appropriate for heavily obscured objects in which even the $f_{60\,\mu m}/f_{25\,\mu m}$ color may be affected by reddening; instead, any such IR–red AGN will be found in the "starburst" sample. In addition, for many AGNs as defined above, much of the IR radiation can be due to the emission of dust heated by stars in the host galaxy in addition to the dust emission associated with the AGN. For example, according to equation (1) of Paper I, an IR source of $f_{60\mu m}/f_{25\mu m} = 5$ (an "AGN" by the above definition) has half of its 25 μm emission from dust heated by stars. In reality, Seyfert galaxies such as NGC 4945 (Spoon et al. 2000) can have the IR emission predominantly powered by the nuclear starburst rather than by the AGN. This explains why the SEDs of some sources in the AGN subsample of our SED library show significant broadband MIR emission features (Fig. 1*a*), which should be absent in a typical type 1 AGN SED (e.g., Fig. 3 of Paper I). At the same time, as shown in Figure 2, the UIB features are indeed absent in the model SEDs of AGNs such as Mrk 231 and NGC 7479, consistent with the fact that the emission in these sources is dominated by the AGN. It should also be noted that in our SED model (Paper I), we do not distinguish type 1 and type 2 AGNs, which have significantly different MIR SEDs (Clavel et al. 2000). Many type 2 AGNs have strong UIB features even when their IR emission may be predominantly from dustassociatedwithAGNbecauseanedge-ontorusmayheavily extinguish the MIR part of the AGN-associated emission and therefore the detected MIR emission is mostly from dust in the ISM of the host galaxy (Clavel et al. 2000).

LFs were then computed for each of these populations according to the maximum likelihood method described in Yahil et al. (1991) and used in Shupe et al. (1998). This method calculates the shape of a parametric LF described by the parameters α, β, and L_* independent of density variations.

With the shape parameters in hand, the normalization of each LF must be estimated by other methods. Since the normalization of the total 25 μm LF was estimated in Shupe et al. (1998), the normalizations of the three population LFs are chosen so that the number of galaxies implied by the sum of the component LFs is about the same as the total LF. The difference between the total LF and summed LF is also constrained to be less than a few percent at all luminosities. We have adjusted the normalizations of the component LFs to satisfy these criteria. These relative weightings of the component LFs can be adjusted by 10%–20% while still satisfying the criteria but cannot be made vastly different from the nominal values.

A plot of the component LFs, the sum of the component LFs, and the total LF is shown in Figure 3. The computed parameters for each population are given in Table 3. Note that the LFs are calculated using the whole sample (1455 galaxies) of Shupe et al. (1998). Identical results are obtained when the sample is confined to the 1406 galaxies with $z < 0.1$.

3.2. *Monte Carlo Simulation of Multiband Surveys*

In this subsection we develop the algorithm to model coherently the number counts in different bands and the color-color diagrams for multiband surveys.

In a flat Λ universe (i.e., $\Omega = \Omega_m + \Omega_\Lambda = 1$, $\Omega_\Lambda \neq 0$), which is adopted in this work, the comoving volume is

$$V = \frac{A}{3} D_M^3 , \tag{1}$$

where A is the sky coverage in steradians and D_M is the proper motion distance (Carroll, Press, & Turner 1992),[5]

$$D_M = \frac{c}{H_0} \int_0^{z1} [(1+z)^2(1+\Omega_m z) - z(2+z)\Omega_\Lambda]^{-1/2} dz . \tag{2}$$

[5] D_A, the angular diameter distance in § 4.1 of Paper I, should have been called D_M, the proper motion distance, too.

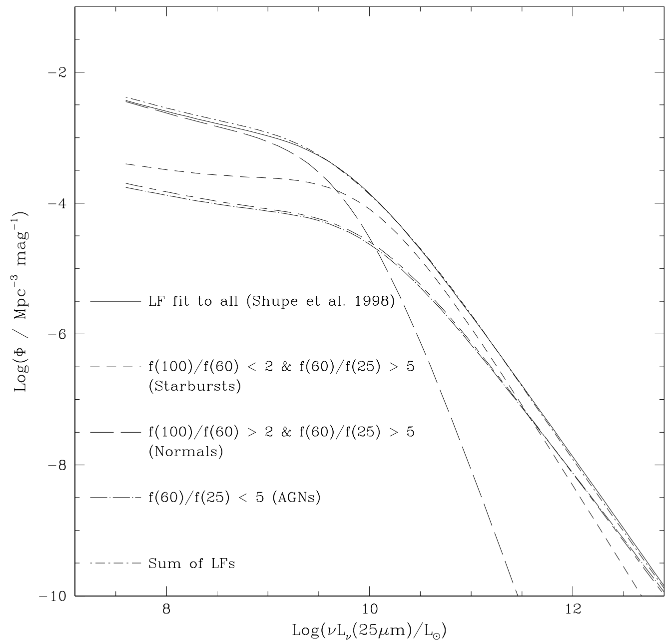

FIG. 3.—LLFs of different populations. The solid line is the LLF of all sources, taken from Shupe et al. (1998). The short-dashed line is the LLF of starburst galaxies ($f_{60\mu m}/f_{25\mu m} > 5$ and $f_{100\mu m}/f_{60\mu m} < 2$). The long-dashed line is the LLF of normal late-type galaxies ($f_{60\mu m}/f_{25\mu m} > 5$ and $f_{100\mu m}/f_{60\mu m} \geq 2$). The dot–long-dashed line is the LLF of galaxies with AGNs ($f_{60\mu m}/f_{25\mu m} \leq 5$). The dot–short-dashed line is the sum of the LLFs of the three populations.

The predicted number of sources from a given population, in a given redshift interval ($z - 0.5\delta z$, $z + 0.5\delta z$), and in a given 25 μm luminosity interval ($L - 0.5\delta L$, $L + 0.5\delta L$) is then

$$\delta N_i(L, z) = \rho_i'(L, z) \frac{dV}{dz} \delta L \, \delta z , \tag{3}$$

where ρ_i' is the LF of population i ($i = 1$: normal late-type galaxies; $i = 2$: starburst galaxies; $i = 3$: galaxies with AGNs),

$$\rho_i'(L, z) = G_i(z) \rho_i \left[\frac{L}{F_i(z)} \right] , \tag{4}$$

where ρ_i is the local 25 μm LF (LF at $z = 0$) of population i (§ 3.1) and $G_i(z)$ and $F_i(z)$ are the density evolution function and the luminosity evolution function of population i, respectively.

For each of the $\delta N_i(L, z)$ sources predicted using equation (3), an SED is randomly selected from a proper SED bin in the SED library (§ 2) and is assigned to the source. The SED library is binned according to (1) the population and (2) the 25 μm luminosity (Table 1). For an individual

TABLE 3

PARAMETERS OF LLFs OF DIFFERENT POPULATIONS

Population	Number	α	β	$L_*/L_\odot$	C(normalization)
Normals	456	0.482	3.876	5.7×10^9	0.00035
Starbursts......	643	0.268	2.230	7.9×10^9	0.00066
AGNs	356	0.336	1.691	6.9×10^9	0.000090

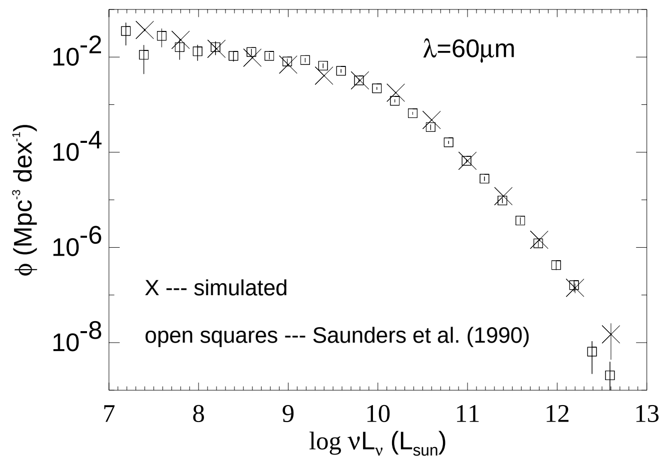

FIG. 4.—LLF of the *IRAS* 60 μm band. Simulation results (*crosses*) compared with the data of Saunders et al. (1990) (*open squares*).

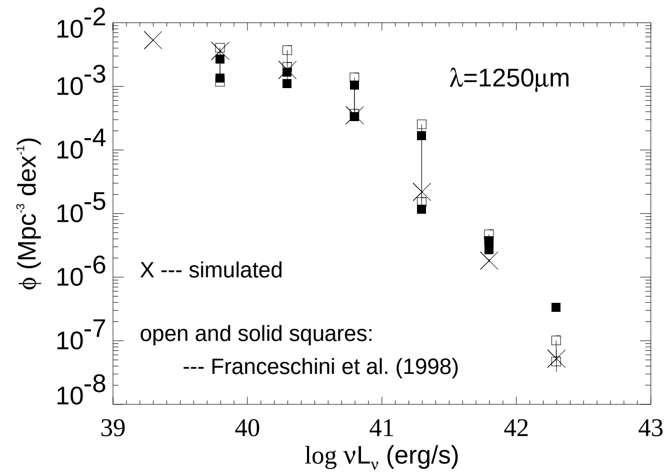

FIG. 6.—LLF of the IRAM 1250 μm band. Simulation results (*crosses*) compared with the data of Franceschini et al. (1998). Open squares and filled squares are results derived from the same data using different methods (Franceschini et al. 1998). For a given luminosity, the difference between the pairs of open and filled squares is due to the different aperture corrections of the 1250 μm flux data.

source the flux density in a given band can then be determined as follows:

$$f_{\rm band} = \frac{1}{4\pi D_L^2}\,\frac{L_{25\ \mu{\rm m}}/25\ \mu{\rm m}}{S(25\ \mu{\rm m})}\int_{\lambda_1}^{\lambda_2} S\left(\frac{\lambda}{1+z}\right) R_{\rm band}(\lambda)d\lambda\ , \quad (5)$$

where

$$D_L = (1+z)D_M \quad (6)$$

is the luminosity distance (Carroll et al. 1992), $L_{25\mu{\rm m}} = \nu L_\nu(25\ \mu{\rm m}) = \lambda L_\lambda(25\ \mu{\rm m})$ is the monochromatic luminosity at 25 μm, $R_{\rm band}(\lambda)$ is the bandpass of the given band, and $S(\lambda)$ is the flux density distribution of the SED in question. As a result of the dependence of SED shape on luminosity for IR bright galaxies (the $f_{60\ \mu{\rm m}}/f_{100\ \mu{\rm m}}$ color increases with $L_{\rm IR}$), this approach empirically results in color evolution accompanying luminosity evolution.

When the evolution functions in equation (4) are specified, we can predict counts in different IR bands, as well as contributions from IR galaxies to counts in other wave bands. As tests local LFs in the *IRAS* 60 μm band (Fig. 4), in the SCUBA 850 μm band (Fig. 5), and in the IRAM 1250 μm band (Fig. 6) are calculated via model simulations (for sources of $z < 0.1$) specified by $G_i(z) = 1$ and $F_i(z) = 1$.

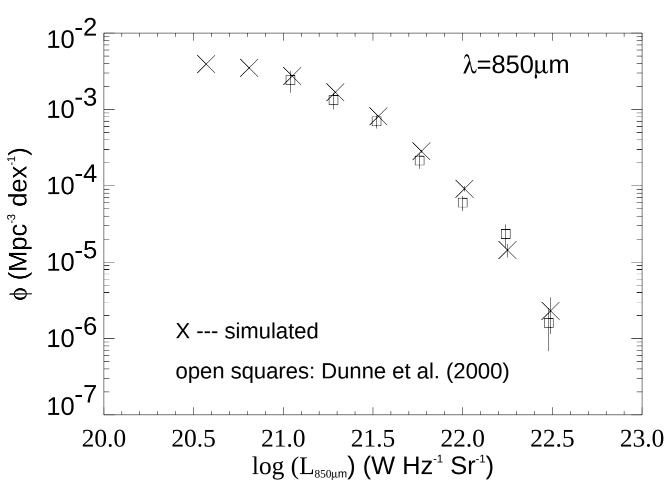

FIG. 5.—LLF of the SCUBA 850 μm band. Simulation results (*crosses*) compared with the data of Dunne et al. (2000) (*open squares*).

Good agreement with the *IRAS* 60 μm LF of Saunders et al. (1990), with the 850 μm LF of Dunne et al. (2000), and with the 1250 μm LF of Franceschini, Andreani, & Danese (1998) is found.

3.3. *Evolution Models*

As in Papers I and II, the following (power-law) function forms are adopted for the luminosity evolution functions $F_i(z)$ and the density evolution functions $G_i(z)$:

$$F_i(z) = \begin{cases} (1+z)^{u_i} & (z \le z_1)\ , \\ (1+z)^{v_i} & (z_1 < z \le z_0)\ , \end{cases} \quad (7)$$

$$G_i(z) = \begin{cases} (1+z)^{p_i} & (z \le z_1), \\ (1+z)^{q_i} & (z_1 < z \le z_0)\ , \end{cases} \quad (8)$$

where z_0 is the redshift when the galaxy formation started and z_1 is the so-called peak redshift, where the evolution reaches a peak. Here we explore two kinds of models, the first characterized by a steady increase in evolution from z_0 to z_1 at power-law rates v_i and q_i followed by a strong decline to the present day with power-law rates u_i and p_i, and the second having a plateau between the formation and peak epochs, $z_0 > z > z_1$.

Throughout the paper we adopt $z_0 = 7$ and $z_1 = 1.5$. Our results (predictions for number counts and the CIB) are not sensitive to z_0 so long as it is greater than 5. Optical surveys (e.g., Lilly et al. 1996; Madau et al. 1996; Connolly et al. 1997) show that star formation rate (SFR) in galaxies peaks between $z = 1$ and 2. The deep ISOCAM counts (e.g., Elbaz et al. 1999) are consistent with a rapidly increasing SFR going back at least to $z \ge 1.5$ (Paper II). The choice of 1.5 for the peak redshift is driven by the deep *ISO* 15 μm data (see Fig. 7). It is still controversial whether the SFR indeed decreases at $z > z_1$, beyond the peak, or flattens (e.g., Steidel et al. 1999; Blain et al. 1999).

Other parameters are u_i, v_i, p_i, and q_i ($i = 1, 2, 3$). In order to reduce further the parameter space, we assume the following:

1. For normal late-type galaxies (Population I): $u_1 = 1.5$, $p_1 = 0$. This corresponds to a pure passive luminosity evolution before the turnover redshift. These galaxies are a major constituent of *K*-band extragalactic source counts, which may be consistent with passive evolution models (Gardener et al. 1997).

2. For galaxies with AGNs (Population III): $u_3 = 3.5$, $p_3 = 0$. Here the assumption of the pure luminosity evolution is based on the studies of the evolution of QSOs in the literature (e.g., Boyle, Shank, & Peterson 1988; Pei 1995; La Franca et al. 2000). Using a maximum likelihood technique, Boyle et al. (1988) found that pure luminosity evolution models of the form $L(z) \propto L_0(1+z)^{\gamma}$ ($\gamma = 3.2 \pm 0.1$) adequately describe the evolution of bright ($M_B < -23$), low-redshift ($z < 2.2$) QSOs. A similar result was found by Pei (1995), with γ in the range of 3.2–3.9. Recently, La Franca et al. (2000) found that results from an ISOCAM 15 μm survey of type 1 AGNs in the European Large-Area *ISO* Survey (ELAIS) fields are consistent with a pure luminosity evolution model with $L(z) \propto L_0(1+z)^{3.4}$.

3. The evolution indices u_2 and p_2, which specify the luminosity and density evolution rate of starburst galaxies before $z = 1.5$, will be the free parameters. Given the results of Paper II on the evolution of deep ISOCAM counts, it is expected that at $z < 1.5$ the starburst galaxies will have a stronger evolution rate than what has been assumed for normal late-type galaxies (assumption [1]) and for galaxies with AGNs (assumption [2]), consistent with the preliminary identifications of faint ISOCAM sources (Flores et al. 1999).

4. Again for the sake of simplicity, we assume that all above-mentioned evolution rates will have the same behavior after $z = z_1$, namely, $v_1 = v_2 = v_3 = q_2$. This is because beyond $z \simeq 1.5$ (the highest redshift detected for *ISO* galaxies), we know very little about the population of IR galaxies.

4. COMPARISONS WITH AVAILABLE SURVEYS AND CONSTRAINTS ON EVOLUTION PARAMETERS

4.1. *Comparisons with ISOCAM 15 μm Band Surveys: Constraints on Evolution of z < 1.5*

In what follows, we will compare our simulations with surveys in different bands found in the literature. The evolution models considered in this paper are listed in Table 4.

We start with the surveys in ISOCAM 15 μm band (Elbaz et al. 1999; Serjeant et al. 2000), where the deepest and the most comprehensive *ISO* surveys have been conducted. As a result of significant effects caused by the UIBs, certain features in the MIR counts can help to constrain the rate of luminosity evolution and that of density evolution separately (Paper I). If the sharp peak at $f_{15\mu\mathrm{m}} \simeq 0.4$ mJy in the Euclidean normalized differential counts is indeed due to the UIBs in 6–8 μm (Paper II), which are redshifted into the 15 μm band when $z \sim 1$, then a 15 μm luminosity of $\sim 10^{11}$ $L_{\odot}$ (νL_{ν} at 15 μm) could be inferred for a typical $z = 1$ ISOCAM galaxy. This imposes a strong constraint to the luminosity evolution rate of the major population of the ISOCAM sources, which under our assumptions (§ 3.3) are the starburst galaxies, at $z \lesssim 1$.

In Figures 7*a* and 7*b*, we compare the simulations of two evolution models: one has $p_2 = 2$, $u_2 = 4.2$, $z_1 = 1.5$, and $v_1 = v_2 = v_3 = q_2 = -3$ (model 1, "peak model"), and the other has $p_2 = 2$, $u_2 = 4.2$, $z_1 = 1.5$, and $v_1 = v_2 = v_3 = q_2 = 0$ (model 2, "flat model"), with the number counts of ISOCAM 15 μm data surveys (Elbaz et al. 1999; Serjeant et al. 2000). Both models fit the *ISO* data very well. Namely, although the "flat model" predicts about a factor of 2 more sources at $f_{15\mu\mathrm{m}} = 0.01$ mJy, there is little difference between the two models above the sensitivity limit of ISOCAM surveys (0.1 mJy). At 0.1 mJy the 15 μm counts are very insensitive to galaxy evolution at $z > 1.5$.

In Figures 7*c* and 7*d* simulations of two other evolution models, model 3 ($p_2 = 1$, $u_2 = 5$, $z_1 = 1.5$, $v_1 = v_2 = v_3 = q_2 = -3$) and model 4 ($p_2 = 3$, $u_2 = 3.5$, $z_1 = 1.5$, $v_1 = v_2 = v_3 = q_2 = -3$), are also plotted. The former assumes more luminosity evolution ($u_2 = 5$) and less density evolution ($p_2 = 1$) for the starbursts at $z < 1.5$. It gives a slightly less good fit to the 15 μm data (Fig. 7*c*), predicting a shallower peak at slightly brighter flux level than that of the data. The latter assumes less luminosity evolution ($u_2 = 3.5$) but more density evolution ($p_2 = 3$) for the starbursts before $z \leq 1.5$. It fits the 15 μm data very well (Fig. 7*d*).

In Figure 8 we compare the redshift distributions predicted by the "peak model" and by the "flat model" with the data. The data of both Aussel et al. (1999) and Flores et al. (1999) are assumed to be complete at the 50% level (i.e., half of the sources are missing from the two plots as a result of a lack of redshifts). By definition (Table 4), the "peak model" and the "flat model" differ only at $z > 1.5$. For the HDF-N survey, the model predicts a slightly higher median z (~ 1) compared to the median of the data ($z \sim 0.7$). However,

TABLE 4

EVOLUTION MODELS

			NORMALS				STARBURSTS				AGNS			
MODEL	z_1	z_0	u_1	v_1	p_1	q_1	u_2	v_2	p_2	q_2	u_3	v_3	p_3	q_3
Model 1[a]	1.5	7	1.5	−3	0	0	4.2	−3	2	−3	3.5	−3	0	0
Model 2[b]	1.5	7	1.5	0	0	0	4.2	0	2	0	3.5	0	0	0
Model 3	1.5	7	1.5	−3	0	0	5	−3	1	−3	3.5	−3	0	0
Model 4	1.5	7	1.5	−3	0	0	3.5	−3	3	−3	3.5	−3	0	0
Model 5	1.5	7	1.5	−1.5	0	0	4.2	−1.5	2	−1.5	3.5	−1.5	0	0

NOTE.—Parameters z_0 and z_1 specify the galaxy formation time and the "turnover" redshift, respectively; u_i and v_i ($i = 1, 2, 3$) specify the luminosity evolution functions (eq. [7]), and p_i and q_i ($i = 1, 2, 3$) specify the density evolution functions (eq. [8]).

[a] "Peak model."

[b] "Flat model."

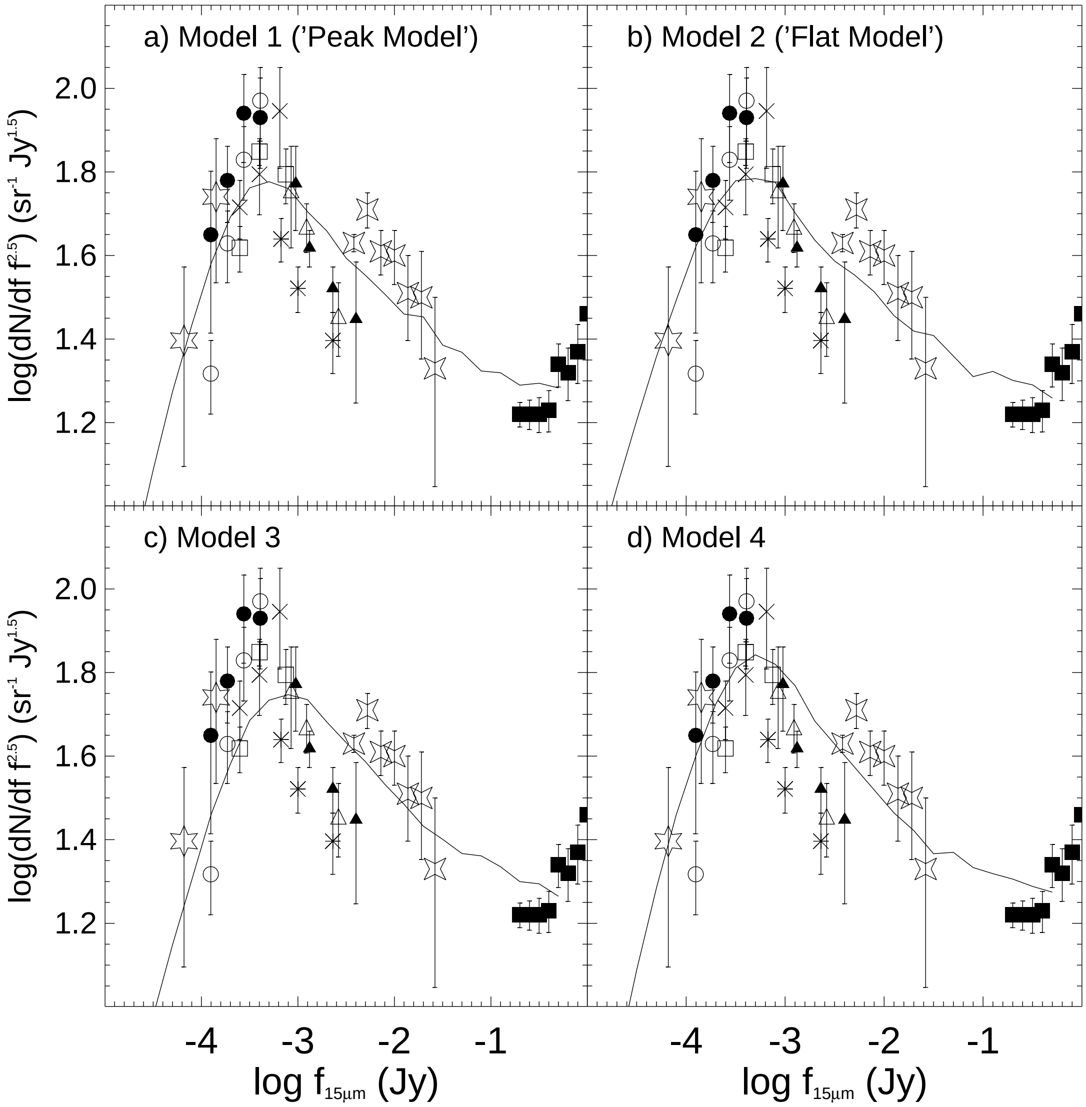

FIG. 7.—Euclidean normalized 15 μm differential counts: model predictions compared to the observations. Simulations of four different models (Table 4) are plotted in the four panels. At the bright end ($\log f_{15\mu m} > -0.7$ Jy) the filled squares are 15 μm counts derived from the 25 μm selected sample using the predicted 15 μm flux densities of the sources (Fig. 4 of Paper II). The new ELAIS data (Serjeant et al. 2000) are plotted with four-point stars (around 10 mJy). Other data points have the same symbols as in Elbaz et al. (1999): A2390 (*six-point stars*); *ISO* HDF-N (*open circles*), *ISO* HDF-S (*filled circles*), Marano FIRBACK Ultradeep (*open squares*), Marano Ultradeep (*crosses*), Marano FIRBACK Deep (*asterisks*), Lockman Deep (*open triangles*), Lockman Shallow (*filled triangles*).

since the redshift data are not complete and the high redshifts are more likely to be missing (more difficult to measure), and since the HDF-N is such a tiny field that any cluster at a given redshift (e.g., at $z \sim 0.7$) can affect the redshift distribution significantly, we feel that this discrepancy is not inconsistent with our models. The CFRS survey is shallower (and wider) than the HDF-N survey, but its redshift distribution is more skewed toward the high-z end, supporting our argument that the z distribution of the ISOCAM sources in the HDF-N field might not be representative for $f_{15\mu m} > 0.1$ sources. The "peak model" predicts a median redshift of 0.75 for the CFRS survey, very close to that of the data.

4.2. *Comparisons with the CIB and the SCUBA 850 μm Band Surveys: Constraints on Evolution of z > 1.5*

Because of the negative *K*-correction in the submillimeter bands, the best constraints on galaxy evolution beyond $z \sim 2$ come from the CIB and the submillimeter counts. Our model predictions for the CIB are derived by summing up the flux densities of all sources in a very deep simulation ($f_{24\mu m} \geq 10^{-9}$ mJy) for the band in question. In Figure 9 we compare the CIB predicted by four different models to the observations. The solid curve is obtained by the "peak model," which fits the CIB very well (except for the 60 μm point of Finkbeiner, Davis, & Schlegel 2000). The dotted curve is the result of the "flat model," which overpredicts the submillimeter CIB substantially (by a factor of ~ 2). The stronger density evolution model in Figure 7*c* (model 4; *dot-dashed curve* in Fig. 9) overpredicts the CIB by $\sim 30\%$–50%. In particular, it marginally violates the upper limits set by the TeV gamma-ray observations (Stanev & Franceschini 1998) in the MIR. Another model (model 5), which is otherwise the same as the "peak model" except for a less steep drop ($v_1 = v_2 = v_3 = q_2 = -1.5$ instead of $v_1 = v_2 = v_3 = q_2 = -3$) after $z = 1.5$, is also plotted in Figure 9

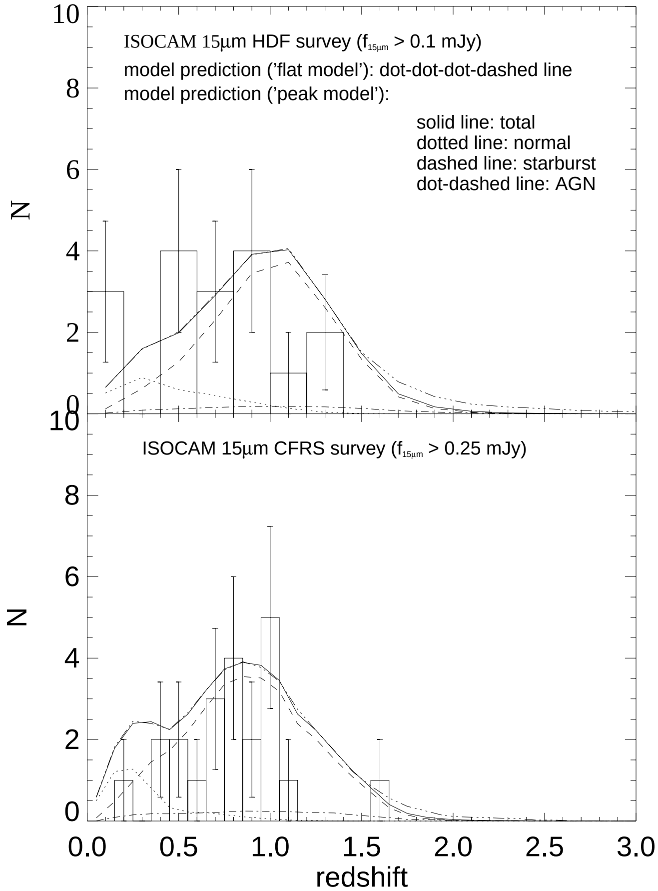

FIG. 8.—Redshift distributions (~50% incomplete) of 15 μm sources in the HDF-N (Aussel et al. 1999; *upper panel*) and in the CFRS field (Flores et al. 1999; *lower panel*) compared to model predictions. In both plots, the triple-dot–dashed lines give the predictions by the "flat model," and the solid lines give the prediction by the "peak model." The "peak model" is further decomposed into (1) normal late-type galaxies (*dotted lines*), (2) starbursts (*dashed lines*), and (3) AGNs (*dot-dashed lines*).

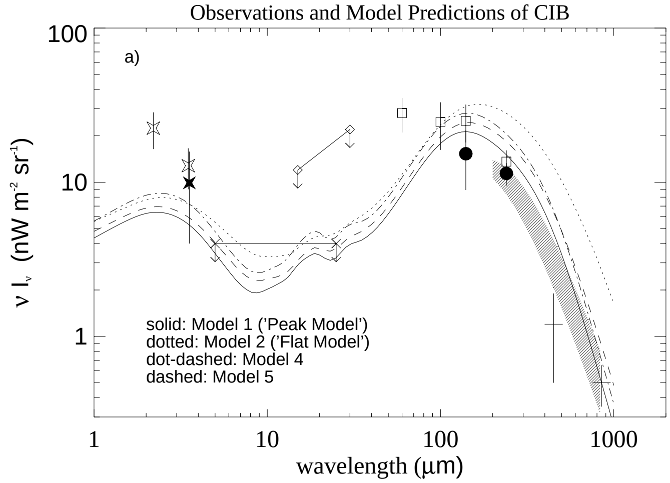

FIG. 9.—Comparisons of predictions of the CIB by different models with the observational data. *Solid line:* "peak model"; *dotted line:* "flat model"; *dot-dashed line:* model 4 in Table 4; *dashed line:* model 5 in Table 4. *Filled circles with error bars: COBE*/DIRBE results of Lagache et al. (1998); *open squares: COBE*/DIRBE results of Finkbeiner et al. (2000); *open stars: COBE*/DIRBE results of Gorjian, Wright, & Chary (2000); *filled star: COBE*/DIRBE result of Dwek & Arendt (1998); *large crosses:* SCUBA source count results (Blain et al. 1999); *shadowed area:* range of *COBE*/FIRAS results (Fixsen et al. 1998); *diamonds and crosses with upper limits:* upper limits from TeV gamma-ray radiation of Mrk 403 and Mrk 501 (Dwek & Slavin 1994; Stanev & Franceschini 1998).

(*dashed curve*). It slightly overpredicts the CIB around 300 μm.

In Figure 10 we compare results from simulations of the "peak model" and of the "flat model" to the 850 μm SCUBA counts. As in the case of the CIB comparisons, the "peak model" fits the data very well, while the predictions of the "flat model" are significantly higher than the data.

4.3. *Comparisons between the Best-Fit Model and the Surveys in Other Bands*

The agreements between the predictions of our best-fit model, the "peak model," and the data from the *ISO* surveys at 90 μm (Fig. 11) and at 175 μm (Fig. 12) are very good. Note that near the faint ends of the 175 μm counts, incompleteness at a level of $\gtrsim$50% is expected (Dole et al. 2000). Corrections for this incompleteness in those data will make the agreement between our model predictions and the data even better.

These good agreements may not be very surprising given that the model plotted here is mostly constrained by fitting the 15 μm survey data (Fig. 7) and that the three FIR bands are linked to the 15 μm band by a SED model that is very robust (§ 2). In Figure 13 the predictions of our best-fit model are compared with the *IRAS* surveys at 60 μm (Fig. 13). Here the data show a large spread, and our model is about 10% higher relative to the data at $\log f_{60} < 0.3$ (Jy) if the Gregorich et al. (1995) data are ignored (they may suffer from overestimation; Bertin et al. 1997). If real, the small overprediction of these bright counts might be a consequence of a high local normalization (e.g., Lonsdale et al. 1990). We will investigate this possibility further in our next paper.

We compare the redshift distribution of *IRAS* 60 μm sources observed by Oliver et al. (1996) and that predicted by our best-fit model in Figure 14. The overall agreement looks quite good. On the other hand, there seems to be a slight excess of data points in the low-z region ($z < 0.014$)

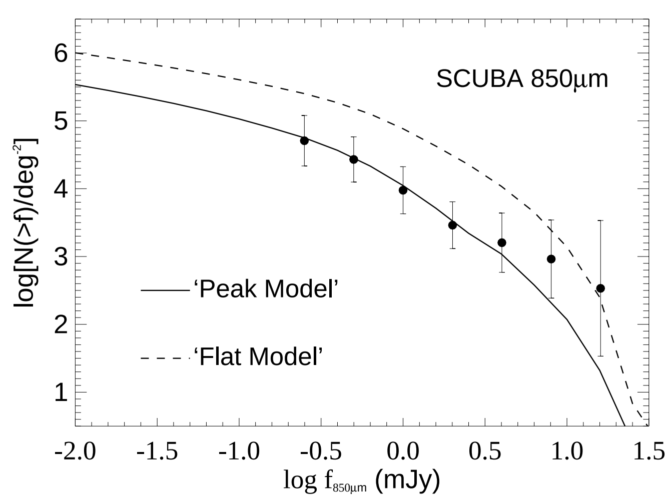

FIG. 10.—Integral counts at 850 μm: model predictions of the "peak model" (*solid line*) and the "flat model" (*dotted line*) compared with the SCUBA data compiled by Blain et al. (2000).

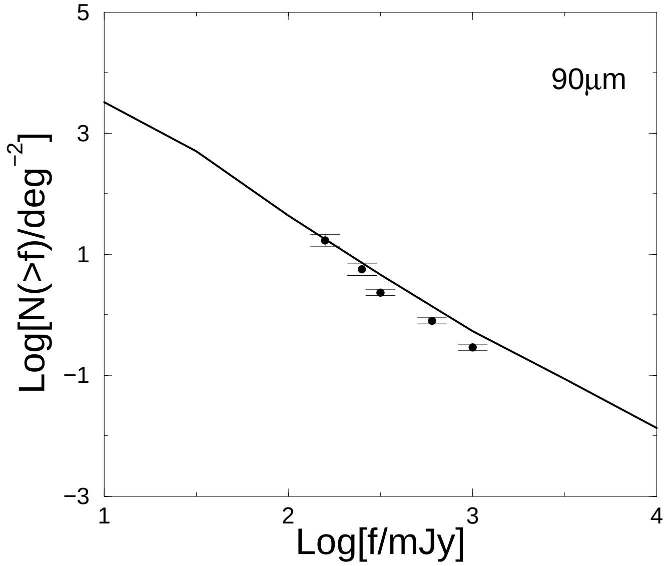

FIG. 11.—Integral counts at 90 μm: comparisons between predictions of the "peak model" and data from ELAIS (Oliver et al. 2000; Efstathiou et al. 2000a).

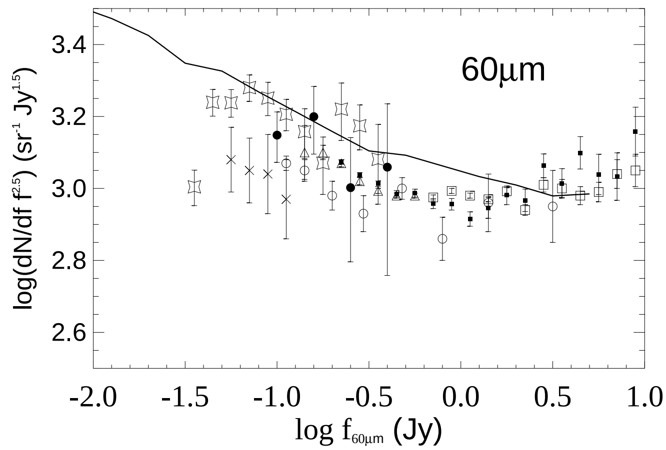

FIG. 13.—Euclidean normalized differential counts of the *IRAS* 60 μm band: model predictions compared to the observations. *Large filled circles:* new north ecliptic pole region (Paper II); *crosses:* Hacking & Houck (1987); *open stars:* Gregorich et al. (1995); *open circles:* Bertin et al. (1997); *small filled squares:* Lonsdale et al. (1990); *open triangles:* Saunders et al. (1990); *open squares:* Rowan-Robinson et al. (1990).

and the opposite in the high-z ($z > 0.033$) region. It is not clear whether these are due to large-scale structures (the amplitudes of the deviations are of the same order as the fluctuations due to the large-scale structures) or they hint that the luminosity evolution rate of the best-fit model is too strong. It is also not clear whether the low fraction of high-z galaxies could be explained, at least partially, by the incompleteness of the redshift survey ($\sim$10%; Oliver et al. 1996). Future deeper surveys will certainly help to answer these questions.

Finally, we present the predicted contributions of IR bright sources to the counts in the NIR K band, the optical B band, and the radio continuum 20 cm band and compare them with survey data from the literature. Again only the predictions of our best-fit model, the "peak model," are considered here. Euclidean normalized differential counts in K band are plotted in Figure 15. Compared to the data points taken from various K-band surveys (Soifer et al. 1994; Gardner et al. 1996; Bershady, Lowenthal, & Koo 1998; Minezaki et al. 1998), the "peak model" predicts that for $K < 22$, about 50%–80% of the sources are IR bright, in reasonable agreement with the fraction of late-type galaxies among K-band sources (Huang, Cowie, & Luppino 1998). It appears that the model prediction is significantly below the counts of $K > 22$, though there are only two data points there. A tentative comparison with *Hubble Space Telescope* (*HST*) NICMOS H-band deep counts (L. J. Storrie-Lombardi 2000, private communication) shows that the "peak model" predicts about 50% of the NIR counts down to $H = 26.5$ mag.

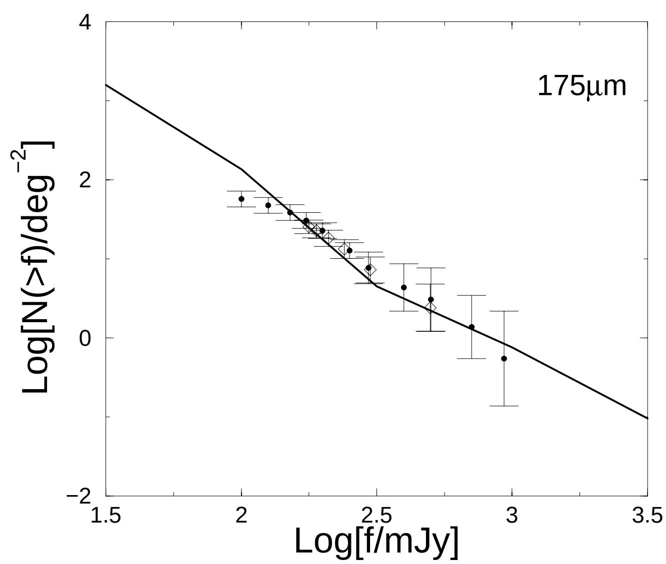

FIG. 12.—Integral counts at 175 μm: comparisons between predictions of the "peak model" and data from the "FIRBACK" survey. *Filled circles:* Dole et al. (2000); *open diamonds:* Dole et al. (2001).

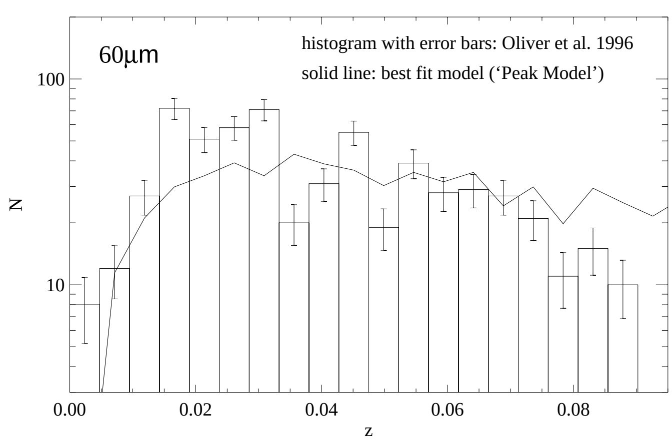

FIG. 14.—Redshift distribution of *IRAS* 60 μm sources: comparisons between predictions of the "peak model" and the observational data, taken from Fig. 5 of Oliver et al. (1996). The flux limit of the survey is $f_{60\mu m} = 200$ mJy, and the sky coverage is taken to be 623 deg^2 ($26°.5 < \delta < 32°.5$, $8^h < \alpha < 16^h$) minus a 20% mask (Oliver et al. 1996), and a correction of 10% incompleteness is included.

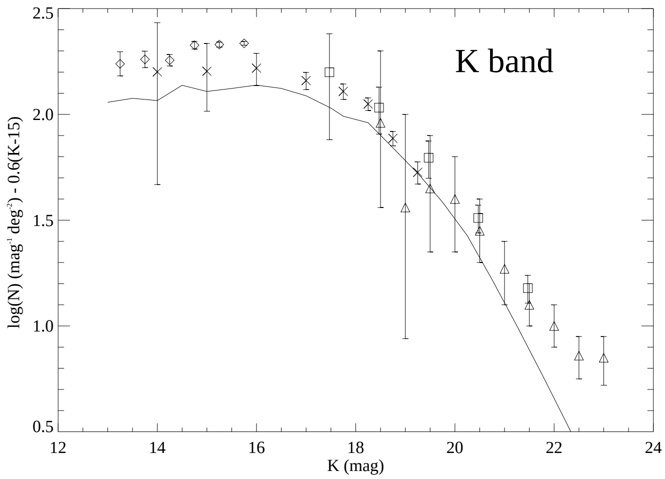

FIG. 15.—Euclidean normalized differential counts in the K band (2.2 μm): comparisons between predictions of the "peak model" (*solid curve*) and the data. *Open triangles:* Bershady et al. (1998); *open squares:* Soifer et al. (1994); *crosses:* Minezaki et al. (1998); *open diamonds:* Gardner et al. (1996). As expected, the IR bright galaxy population underpredicts the K-band counts.

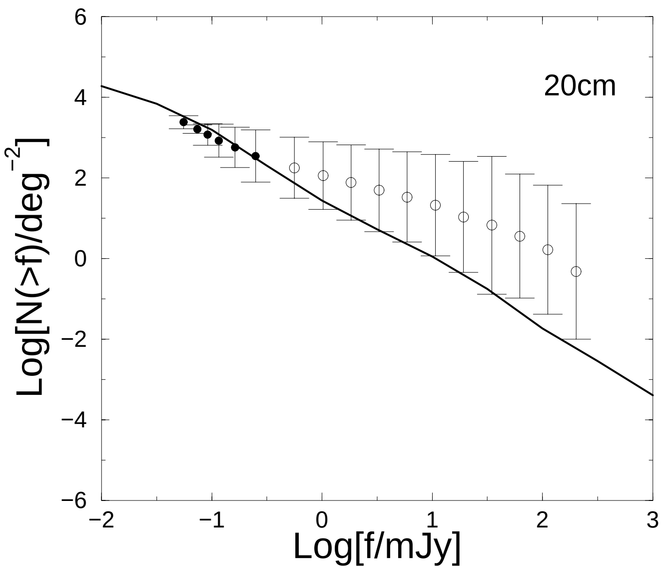

FIG. 17.—Integral counts at 20 cm (1.4 GHz): comparisons between predictions of the "peak model" and deep VLA data from Ciliegi et al. (1999) (*open circles*) and Richards et al. (1999) (*filled circles*).

In Figure 16 we compare predicted contributions from IR sources to the B-band counts. Since the E/S0 galaxies constitute only $\sim 20\%$ of the optical galaxies (Glazebrook et al. 1995), which is a general result holding even for a very faint sample down to $m_I \simeq 24.25$ mag (Driver et al. 1995), IR bright sources should dominate the B-band counts. The discrepancy near the bright end ($B \sim 15$) could be explained by the local density enhancement (local supercluster). At the faint end ($B > 25$), the "peak model" also slightly underpredicts the counts by $\sim 50\%$. It should be noted that at these faint B-band flux levels, where many sources have high redshifts and the B-band flux is actually due to the rest-frame UV emission, the model predictions suffer large uncertainties because the UV SEDs used in the calculation are not well constrained (§ 2). This will be the focus of our next paper.

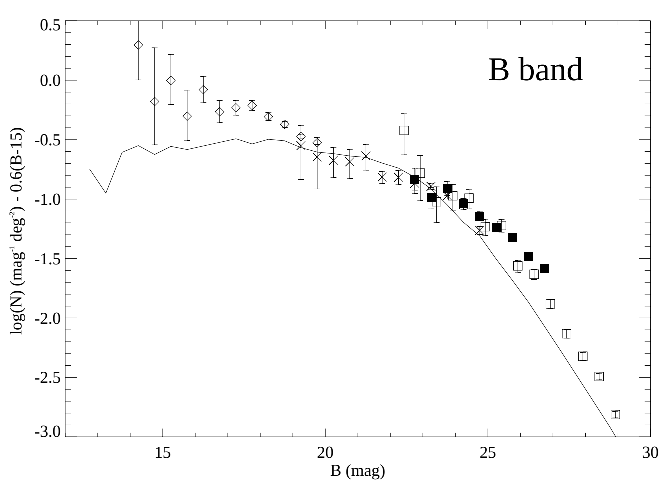

FIG. 16.—Euclidean normalized differential counts in the B band (0.44 μm): comparisons between predictions of the "peak model" (*solid curve*) and data. *Open squares:* Williams et al. (1996); *filled squares:* Metcalfe et al. (1995); *crosses:* Metcalfe et al. (1991); *open diamonds:* Gardner et al. (1996).

In the radio continuum 20 cm band, the bright sources (brighter than 1 mJy) are mostly due to the early-type radio galaxies (Condon 1984), which are not IR emitters, while the faint, submillijansky sources are mostly late-type galaxies (Condon 1984). This is indeed what the "peak model" predicts (Fig. 17): at flux levels brighter than 1 mJy, the IR sources contribute less than 10% of radio counts. At faint flux levels (~ 0.1 mJy), they can fully account for the radio counts.

5. PREDICTIONS FOR MULTIBAND *SIRTF* SURVEYS

5.1. *Number Counts and Confusion Limits*

In this section we will make predictions using our best-fit model ("peak model"). We will concentrate on future surveys with *SIRTF*, which will be launched in mid-2002. All three MIPS bands (24, 70, 160 μm) and all four IRAC bands (3.6, 4.5, 5.8, and 8 μm) are considered. For the sake of simplicity, we assume that all *SIRTF* bandpasses are 10% ($\lambda/\delta\lambda = 10$).[6] We note that, since the E/S0 galaxies are not included in the model, we may significantly underpredict the counts in the IRAC bands, particularly for the shorter wavelength bands (i.e., the 3.6, 4.5, and 5.8 μm bands). Therefore, our predictions for the counts and the confusion limits in these bands should be treated as lower limits.

In Figure 18 we plot the predicted integral counts for the three MIPS bands and three IRAC bands (3.6, 5.8, and 8 μm). In all MIPS bands, the counts are dominated by the starburst component (including any heavily obscured AGN). In the IRAC bands, normal spirals and galaxies with AGNs give significant contributions to counts brighter than 0.3 mJy (in the 3.6 and 5.8 μm bands they outnumber the starbursts). At fainter flux levels (less than 0.1 mJy) the starburst component dominates the counts in the IRAC bands as well.

[6] See the *Space Infrared Telescope Facility* (*SIRTF*) Observer's Manual (Version 1.0) for details of *SIRTF* instruments.

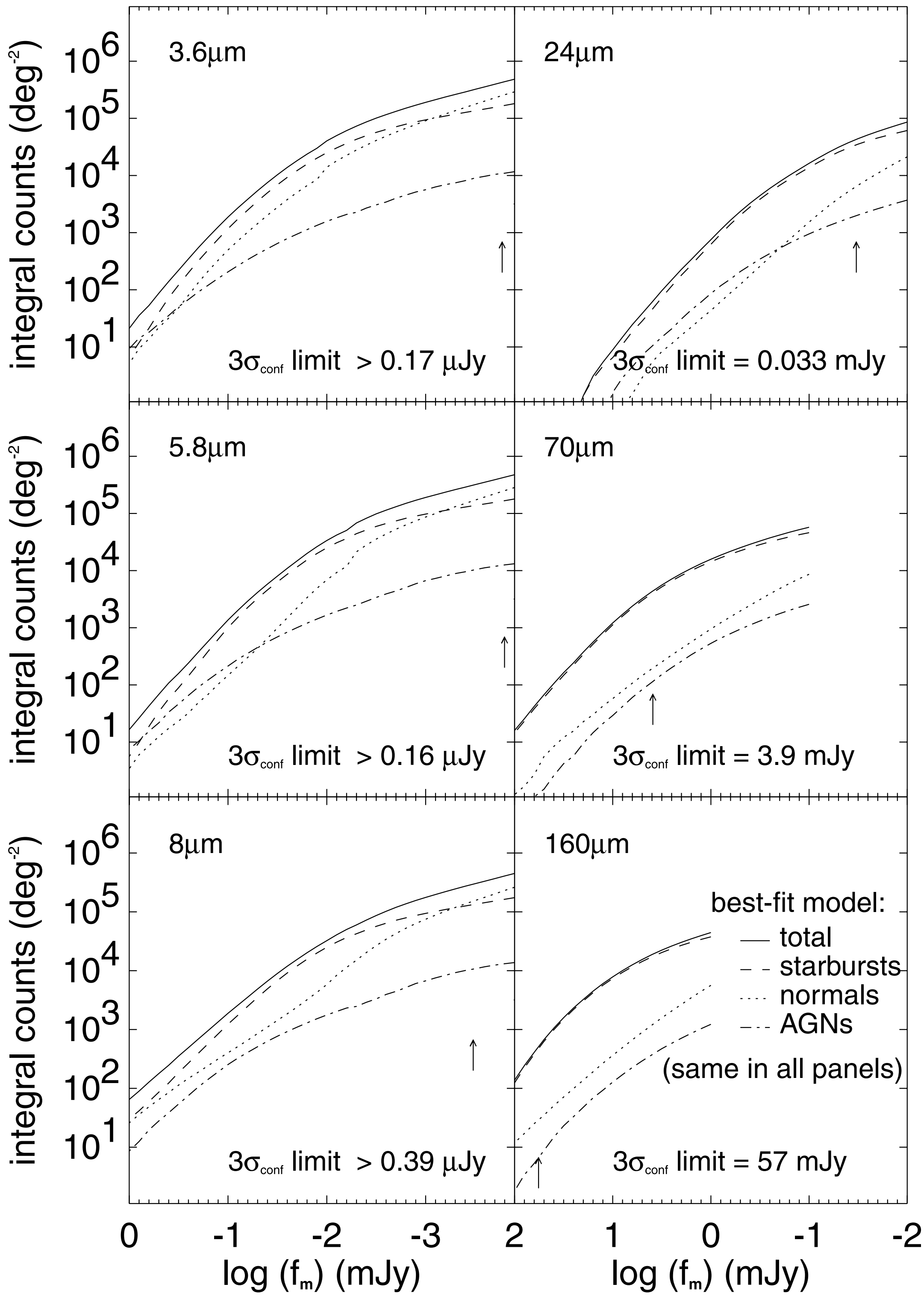

FIG. 18.—Predictions of the "peak model" for integral counts in six *SIRTF* bands. The solid line represents the total counts predicted by the model. Other lines denote contributions of different populations to the total. *Dashed line:* starbursts; *dotted line:* normal late-type galaxies; *dot-dashed line:* AGNs. The small arrow in each plot marks the predicted 3 σ confusion limit. For IRAC bands (*left three panels*), the counts and the confusion limits should be treated as lower limits because of the omission of E/S0 galaxies in the model.

Confusion limits shown in Figure 18 have been computed from the predicted number counts, assuming parameters appropriate for *SIRTF*. The method used is the same as that used by Hacking & Soifer (1991), namely, summing (in quadrature) the contributions from all sources fainter than the limit within the beam, via numerical integration of equation (19) in Hacking & Houck (1987). An Airy function computed from the nominal wavelength is used for the beam. For wavelengths greater than 6 μm, a telescope diameter of 85 cm is used in accordance with the required diffraction-limited performance of the *SIRTF* telescope. For wavelengths shorter than 6 μm, an effective telescope diameter is used to make the beam size larger. Specifically, an effective diameter of 82 cm is used for 5.8 μm, and 51 cm is used for 3.6 μm. As noted above, the confusion limits for the short-wavelength IRAC bands such as the 5.8 and 3.6 μm bands should be treated as lower limits because of the omission of the contribution from counts due to E/S0 galaxies. Also for the MIPS 160 μm band, confusion caused by Galactic cirrus may be significant, especially in high cirrus regions (Gautier et al. 1992; Helou & Beichman 1990).

In Figure 19 redshift distributions predicted by the best-fit model ("peak model") and the "flat model" are plotted. For a 24 μm survey limited at $f_{24\mu m} = 0.055$ mJy ($5\sigma_{\rm conf}$), the best-fit model predicts a prominent peak at about $z = 1$. The starburst component overwhelmingly dominates the counts at $z > 0.5$, while the normal galaxies dominate the low-z end. The contribution from galaxies with AGNs is never important (less than 10%), although it could be significantly higher for obscured AGNs classified here as "starbursts" as a result of their colors. The shape of the redshift distribution predicted by the "flat model" is very different, with a second peak at $z \sim 2$, caused mainly by the prominent UIB features between 6 and 8 μm (Paper I). This peak is cut off in the "peak model" because of the steep decrease of the SFR at $z > 1.5$. However, the turnover redshift z_1, which has been assumed to be 1.5 in all our models presented here, is poorly constrained because *ISO* surveys are too shallow whereas the SCUBA and CIB are more sensitive to sources at $z > 3$. If in reality $z_1 > 2$, then it will be revealed by the second peak at $z \sim 2$ in the redshift distribution of *SIRTF* 24 μm sources.

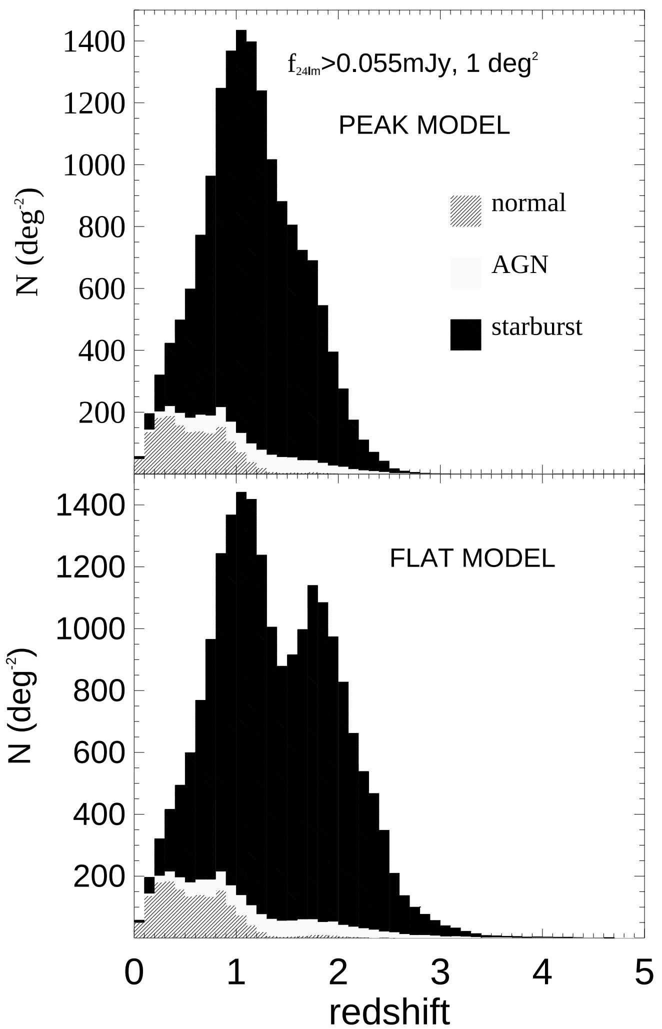

FIG. 19.—Predicted redshift distributions of *SIRTF* surveys with $f_{24\mu m} \geq 0.055$ mJy. *Upper panel:* "peak model." *Lower panel:* "flat model."

5.2. *SIRTF* Color-Color Diagrams

In Figures 20*a* and 20*b* we plot the $f_{24\,\mu m}/f_{8\,\mu m}$ versus $f_{70\,\mu m}/f_{24\,\mu m}$ color-color diagrams predicted by the "peak model" and the "flat model," respectively. Simulations of both models are confined to 1 deg^2 with the following flux limits: $f_{24\mu m} \geq 0.055$ mJy ($5\sigma_{\rm conf}$) and $f_{70\mu m} \geq 2.6$ mJy ($2\sigma_{\rm conf}$). Some general trends are visible in these plots. Galaxies with AGNs are mostly in the relatively low $f_{70\,\mu m}/f_{24\,\mu m}$ ratio region [log ($f_{70\mu m}/f_{24\mu m}$) $\lesssim 1$)], while starburst galaxies dominate the high $f_{70\,\mu m}/f_{24\,\mu m}$ ratio region [log ($f_{70\mu m}/f_{24\mu m}$) $\gtrsim 1$)]. Normal galaxies, with relatively low luminosities and therefore seen only with $z < 1$, are concentrated in the low $f_{24\,\mu m}/f_{8\,\mu m}$ ratio region. It should be pointed out that these trends are closely related to our definitions of the three populations (§ 2), which are separated according to the *IRAS* color ratios of $f_{60\,\mu m}/f_{25\,\mu m}$ and $f_{25\,\mu m}/f_{12\,\mu m}$. While the criteria adopted are based on empirical correlations (Fang et al. 1998; Paper I), the clear boundaries in the definitions of the different populations will have artificially enhanced the trend shown here.

In Figures 21*a* and 21*b* we plot the predictions by the same two models for the MIPS color-color diagram, namely, $f_{160\,\mu m}/f_{70\,\mu m}$ versus $f_{70\,\mu m}/f_{24\,\mu m}$. The symbols are the same as in Figure 20. In these plots, in addition to the flux cutoffs of $f_{24\mu m} \geq 0.055$ mJy and $f_{70\mu m} \geq 2.6$ mJy, it is also required that $f_{160\mu m} \geq 38$ mJy ($2\sigma_{\rm conf}$). The simulations cover 10 deg^2. Most high-z galaxies (*large crosses*) are concentrated in the high $f_{160\,\mu m}/f_{70\,\mu m}$ end [log ($f_{160\mu m}/f_{70\mu m}$) $\gtrsim 0.7$], as a result of the *K*-correction effect associated with the curvature in the 20–160 μm wavelength range in most of the SEDs in our library.

The apparent "tracks" in these figures are a result of the manner in which an SED is selected for each simulated galaxy from the SED library. As luminosity increases with increasing z (for luminosity evolution models), a model galaxy is assigned a random SED from the relevant luminosity bin. Some bins contain small numbers of SEDs, so the "tracks" reflect single SEDs randomly assigned to model galaxies at higher and higher z (and therefore L). The "tracks" can discontinue when model populations "jump" to higher SED library luminosity bins. Although small random scatter could be incorporated into these model colors, we have chosen not to do that so that the figures can be more easily analyzed.

The IRAC color-color diagrams, such as the $f_{4.5\,\mu m}/f_{3.6\,\mu m}$ versus $f_{8\,\mu m}/f_{5.8\,\mu m}$ diagram, are affected by the exclusion of E/S0 galaxies in our current models. In addition, the NIR spectral features considered by Simpson & Eisenhardt (1999), e.g., the 1.6 μm H^- opacity minimum and the 2.3 μm CO band head, are not considered in our SED model (§ 2), therefore the changes in the IRAC colors due to the *K*-correction caused by these features are absent in our model predictions. Improvements in these aspects will be addressed in our next paper.

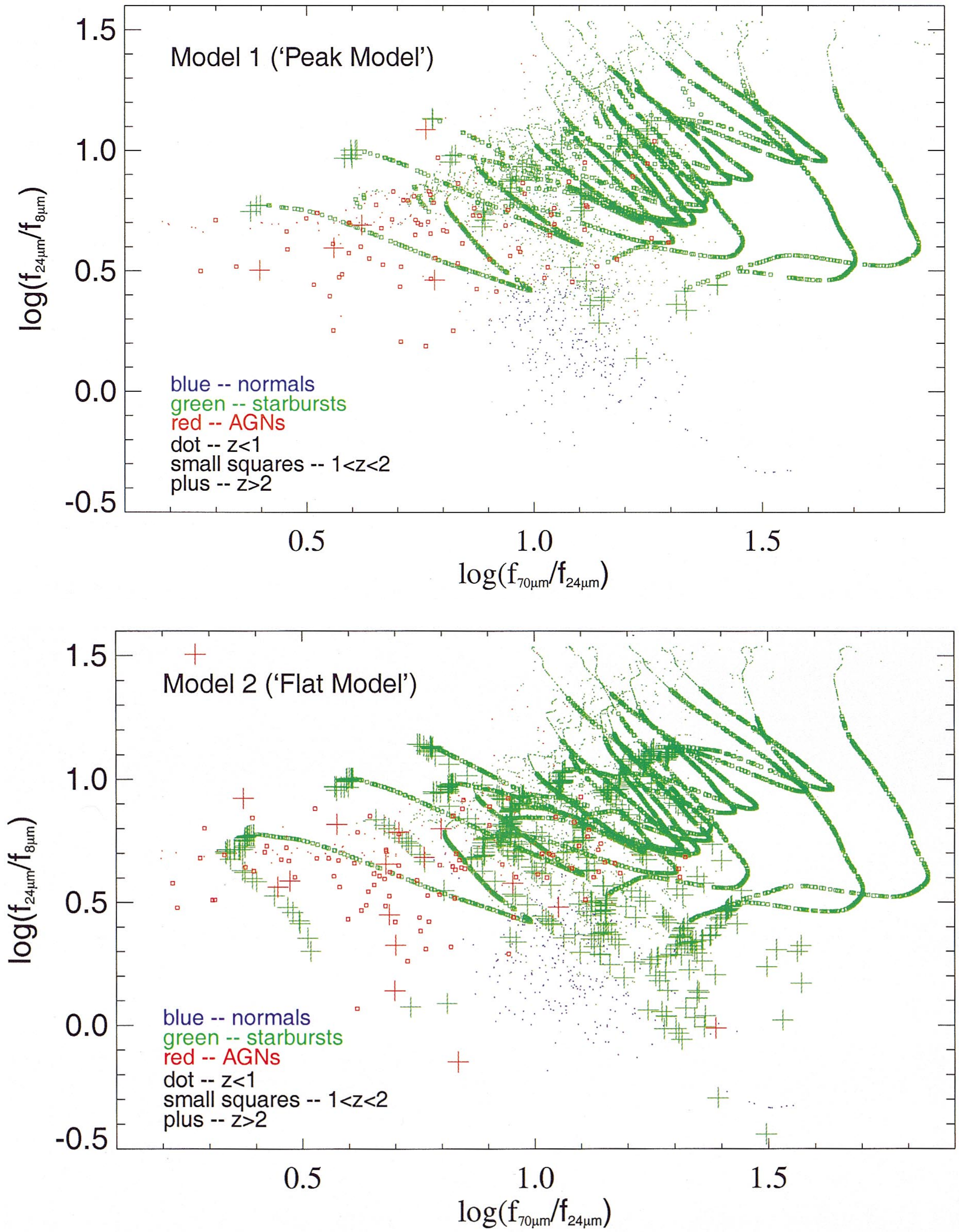

FIG. 20.—Predicted $f_{24\ \mu m}/f_{8\ \mu m}$ vs. $f_{70\ \mu m}/f_{24\ \mu m}$ color-color diagram. *Upper panel:* Predictions by the "peak model." *Lower panel:* Predictions by the "flat model." Both simulations are confined to 1 deg^2 with the following flux limits: $f_{24\mu m} = 0.055$ mJy and $f_{70\mu m} = 2.6$ mJy. Sources of different populations and different redshifts are denoted by different colors and different symbols, respectively.

6. DISCUSSION

6.1. *Comparisons with Previous Models in Literature*

6.1.1. *Comparisons with Models in Papers I and II*

Three new features separate the models presented here from the previous models in Papers I and II:

1. An approach even more empirical than that used in Paper I is adopted in this work. Realistic SEDs of local galaxies are attached to sources of all redshifts. This not only enabled reliable K-corrections but also linked the surveys in different bands coherently. Because of this feature, our model is the first in the literature that can predict the correlations and the dispersions in color-color diagrams for multiband surveys.

2. The MIR to FIR SEDs in the SED sample are extended to a much wider range covering from UV (1000 Å) to radio (20 cm). This links the model predictions for IR surveys to the optical and radio continuum surveys. Because of the wide wavelength coverage, our model can

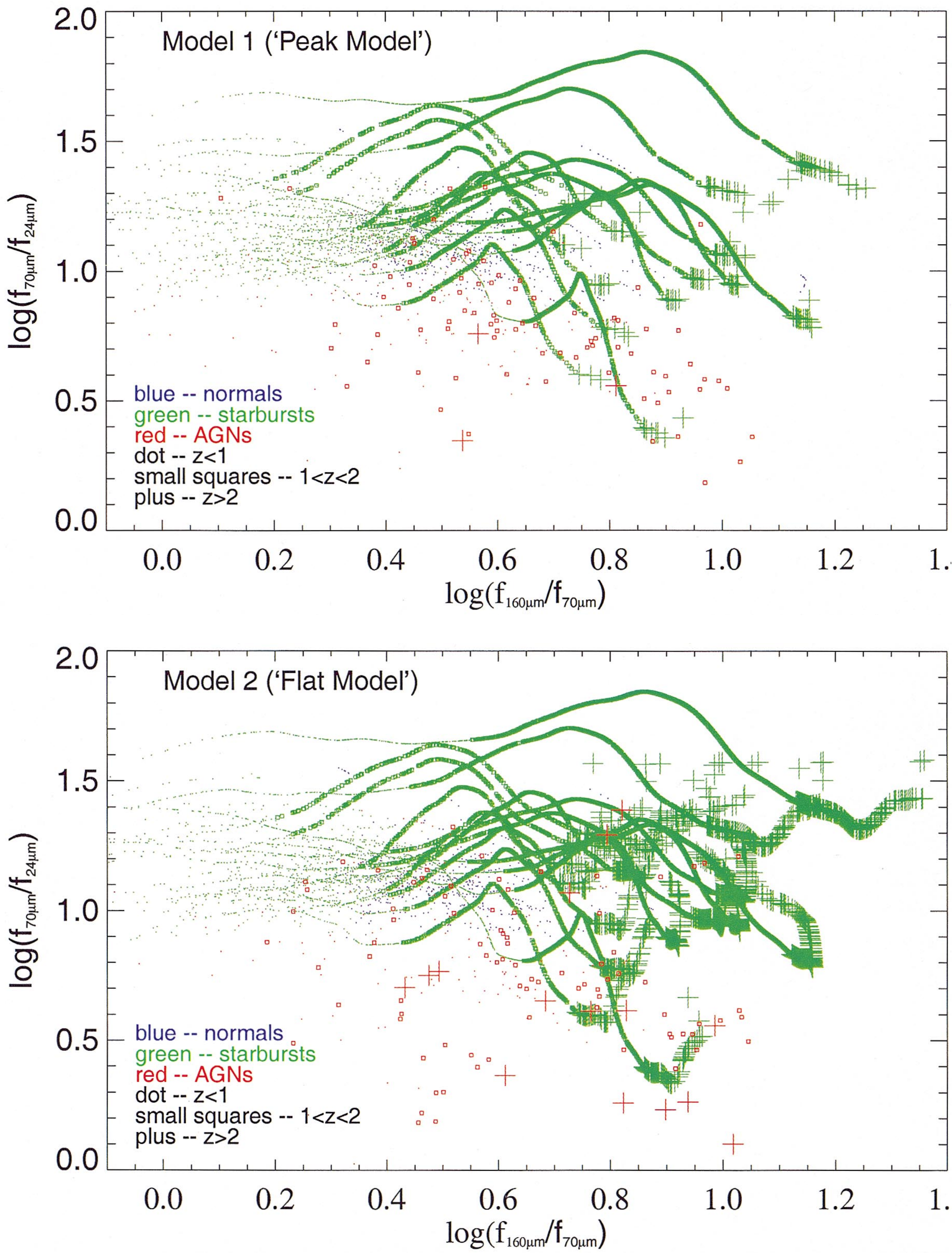

FIG. 21.—Predicted $f_{160\,\mu m}/f_{70\,\mu m}$ vs. $f_{70\,\mu m}/f_{24\,\mu m}$ color-color diagram (MIPS color-color diagram). *Upper panel:* Predictions by the "peak model." *Lower panel:* Predictions by the "flat model." Both simulations are confined to 10 deg^2 with the following flux limits: $f_{24\mu m} = 0.055$ mJy, $f_{70\mu m} = 2.6$ mJy, and $f_{160\mu m} = 38$ mJy. Sources of different populations and different redshifts are denoted by different colors and different symbols, respectively (as in Fig. 20).

calculate the contributions from the IR sources to the cosmic background from optical to radio bands.

3. Instead of evolving all IR sources as a single population, they are divided into three populations (normal late-type galaxies, starbursts, and galaxies with AGNs), which are assumed to evolve differently. Given the observational evidence (Aussel et al. 1999; Elbaz et al. 1999; Flores et al. 1999), most of the evolution is attributed to the starburst (interacting) galaxies.

In Paper II, it was found that a pure luminosity evolution of the form $L \propto (1 + z)^{4.5}$ ($z \leq 1.5$) can fit the ISOCAM 15 μm surveys and *IRAS* 60 μm surveys best (both surveys are insensitive to the evolution at $z > 1.5$). This evolution rate is significantly stronger than those derived in previous *IRAS* studies [$L \propto (1 + z)^3$], while at same time it confirms that luminosity evolution models fit the data better than density evolution models (e.g., Pearson & Rowan-Robinson 1996).

In this paper, while assuming that normal late-type galaxies and galaxies with AGNs undergo pure luminosity evolution [$L \propto (1+z)^{1.5}$ and $L \propto (1+z)^{3.5}$, respectively], we found that a model assuming that both the luminosity and the density of starburst galaxies evolve significantly [$L \propto (1+z)^{4.2}$ and $\rho \propto (1+z)^2$] before the turnover redshift ($z = 1.5$) fits the data best. A model with more luminosity evolution and less density evolution [$L \propto (1+z)^5$ and $\rho \propto (1+z)$] predicted a peak in the Euclidean normalized differential counts at 15 μm too shallow and too bright compared to the data (Fig. 7*c*). Another model with less luminosity evolution and more density evolution [$L \propto (1+z)^{3.5}$ and $\rho \propto (1+z)^3$], while fitting well the 15 μm counts, predicted too much IR background (Figs. 7*d* and 9).

The prediction of our best-fit model of a density evolution of starburst galaxies on the order of $(1+z)^2$ is consistent with the theoretical prediction (Carlberg, Pritchet, & Infante 1994) and with previous observations (Infante, de Mello, & Menanteau 1996; Roche & Eales 1999; Le Févre et al. 2000) of the evolution of merger rate. It is also very consistent with the close relation between starbursts and galaxy interactions/mergers (see Sanders & Mirabel 1996 for a review).

The constraints on the evolution of IR sources at $z > 1.5$ are set by the CIB and the 850 μm SCUBA counts. Because of the negative *K*-correction, high-redshift galaxies contribute significantly to the source counts and the cosmic background in the submillimeter bands. It is found that in order to avoid overpredicting the CIB and the SCUBA counts, a steep decrease after $z = 1.5$, in the form of $(1+z)^{-3}$, in the evolution of IR sources is required. This is different from the result in Paper II, where the "flat model" (luminosity and density remain constant after $z = 1.5$) can fit the CIB satisfactorily (Fig. 7 of Paper II). This is due to the difference in the submillimeter SEDs adopted in these two papers. In Paper II a single template for the submillimeter SEDs is adopted for all sources, specified by $T = 40$ K and $\beta = 1.5$ (Blain et al. 1999). In this paper the submillimeter SEDs are determined using empirical correlations between *IRAS* fluxes and the submillimeter fluxes. This results in a higher submillimeter luminosity for a given MIR luminosity ($L_{24\,\mu\mathrm{m}}$). Since little is known about the IR to submillimeter SEDs of high-*z* sources and we cannot test our assumption that the correlations between the IR and submillimeter fluxes of local galaxies can be applied to high-*z* galaxies, the rapid decrease of the SFR predicted by our best-fit model is highly uncertain.

Because of the steep decrease after $z = 1.5$, our best-fit model predicts a redshift distribution with a single peak at $z \sim 1$ for a survey with $f_{24\mu\mathrm{m}} = 0.055$ mJy ($5\sigma_{\mathrm{conf}}$). This is very different from the double-peaked distribution predicted by the "flat model" (Fig. 19; see also Fig. 14*c* of Paper I). This provides a straightforward test to distinguish these models once the redshifts of a sample of *SIRTF* 24 μm sources are obtained.

6.1.2. *Comparisons with Roche* & Eales (1999)

In the multiband IR model of Roche & Eales (1999), a density evolution of $\rho \propto (1+z)^2$ is also assumed. However, the luminosity evolutionary rate of starburst galaxies found by Roche & Eales (1999), $L \propto (1+z)^2$ ($z < 1$), is significantly weaker than predicted by our best-fit model: $L \propto (1+z)^{4.2}$ ($z < 1.5$).

6.1.3. *Comparisons with Dole et al.* (2000)

Compared to the other two populations (normal late-type galaxies and galaxies with AGNs), our best-fit model predicts much stronger evolution for $z < 1.5$ in the starburst galaxy population. This is similar to the model of Dole et al. (2000). However, they confine their starburst component, called "ULIRGs," to galaxies with greater than 2×10^{11} $L_{\odot}$. In order to fit the *ISO* counts, they have to evolve the ULIRG population significantly, resulting in a "break" in the evolved LF at $z = 2.5$ (Fig. 3*a* of Dole et al. 2000). In Figure 22 the evolved LFs predicted by our best-fit model are plotted. At $z \geq 1$, the starburst component dominates the LF in the whole luminosity range (10^7–10^{12}). Our model does not predict a break such as presented in the model of Dole et al. (2000).

6.1.4. *Comparisons with Blain et al.* (1999)

Blain et al. (1999) used *IRAS* 60 μm counts, early results of *ISO* 175 μm counts, SCUBA 850 μm counts, and the CIB to constrain several families of models for the evolution of IR sources. Since different cosmologies are used ($\Omega_m = 0.3$, $\Omega_\Lambda = 0.7$ in this work; $\Omega_m = 1$, $\Omega_\Lambda = 0$ in Blain et al. 1999), it is difficult to make a quantitative comparison. In the three panels in Figure 23, we plot the cosmic luminosity density evolution from our best-fit model. In the upper panel, the MIR luminosity density, calculated using the parameters of the best-fit model, is plotted versus the time since the big bang (in fraction of the age of the universe t_0). In the middle panel, the density of bolometric luminosity (0.1–1000 μm) obtained from a simulation ($f_{24\mu\mathrm{m}} > 10^{-9}$ mJy, 0.01 deg^2) based on the best-fit model is plotted. In the lower panel, results for the density of IR luminosity (3–1000 μm) from the same simulation are plotted. For IR sources, the IR luminosity density is proportional to the SFR per unit cosmic comoving volume.

Comparing the lower panel of Figure 23 with Figure 9 of Blain et al. (1999), our best-fit model is closer to their "peak models" (rise-peak-drop) than the "anvil models" (rise-peak-flat). As pointed out by Blain et al. (1999), if indeed the contributions from AGNs to the CIB and to the submillimeter counts are negligible, the "peak models" are favored because the "anvil models" may overpredict the metal contents of the universe.

6.1.5. *Comparisons with R01*

Recently, R01 developed a model to study the evolution of galaxies using multiband IR surveys. This goal is similar to that which motivated this paper. Consequently, there are many similarities between R01 and the work presented here:

1. Strategy: both R01 and we use all the available surveys to constrain the evolution and then use the best-fit model to make predictions for future surveys.
2. Methodology: both R01 and we use local SEDs to link all surveys together, though R01 started from the *IRAS* 60 μm band and we started from the *IRAS* 25 μm band.
3. Results: the models of both R01 and this paper can fit all *ISO* surveys, SCUBA 850 μm surveys, and the CIB.
4. These agreements are the natural consequence of the fact that in both papers the model parameters are tuned to fit the counts in these bands. In Figure 24*a*, a comparison between the model predictions on the cosmic luminosity density evolution by R01 (the model for $\Lambda = 0.7$; *triple-dot–*

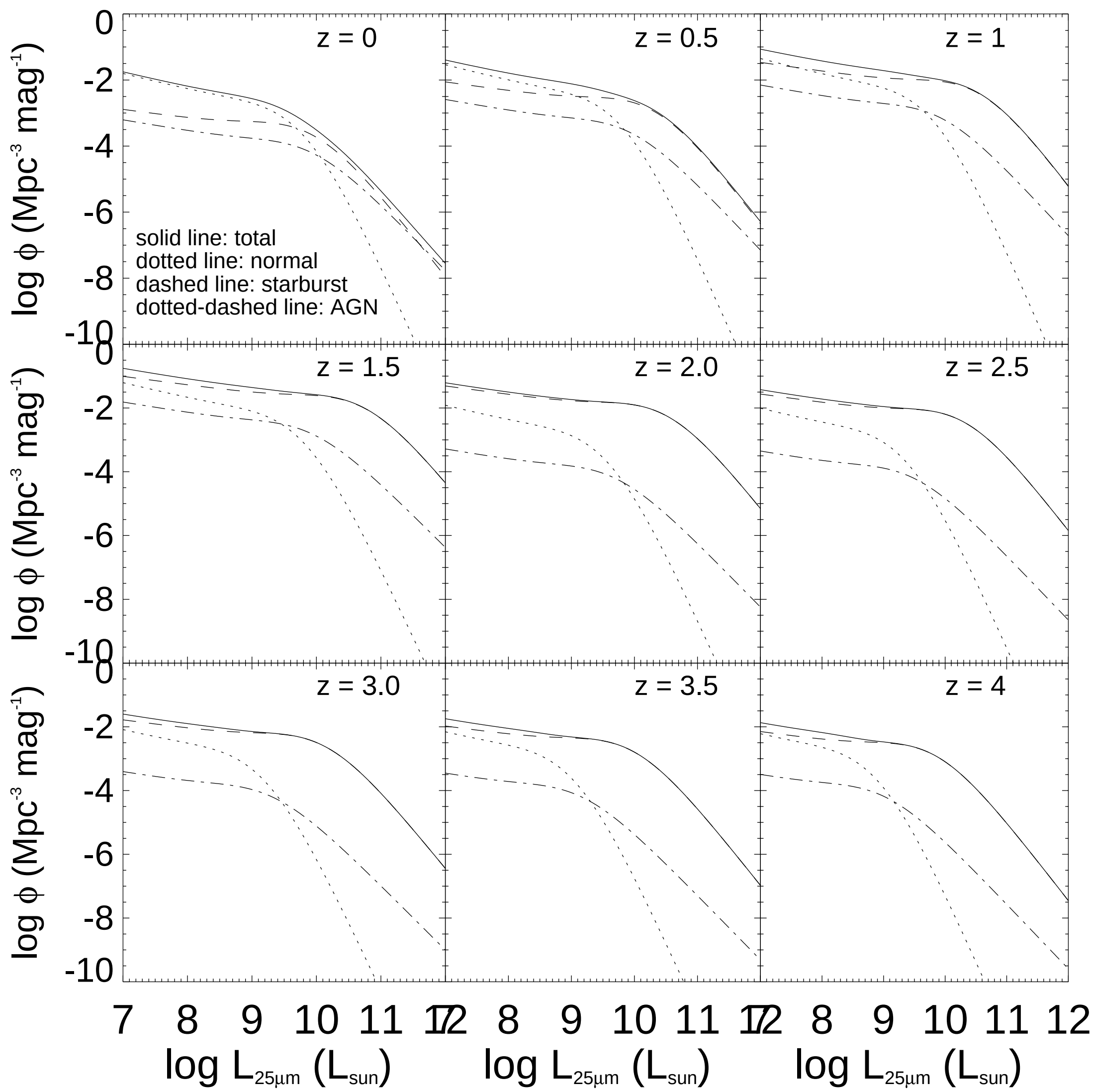

FIG. 22.—Evolution of the 25 μm LF of different populations predicted by the best-fit model ("peak model")

dashed curve) and by our best-fit model ("peak model"; *solid curve*) is plotted. Though the function forms are different, the overall trends are quite similar.

On the other hand, there are some major differences between R01 and this paper:

1. Assumptions: R01 assumed that all the IR sources in his model, which he decomposed into four spectral components (cirrus, M82-like starburst, Arp 220–like starburst, and AGN dust torus), evolve as a single population. We have assumed that the three populations (normal late-type galaxies, starbursts, and galaxies with AGNs) in our model evolve differently. R01 also adopted a different functional form (exponential) to describe the evolution, while the evolution functions in this paper are simple power laws.

2. SEDs: we have used 800 plus empirically determined SEDs, which are binned according to population and luminosity, to constrain the K-corrections and the links between counts in different bands. This is more sophisticated than the approach of R01, where four theoretical SEDs taken from the literature (Efstathiou, Rowan-Robinson, & Siebenmorgen 2000b; Yoshii & Takahara 1988) are adopted for the four populations, respectively.

3. Evolution of SEDs: in R01 models, the SEDs of IR sources undergoing luminosity evolution do not evolve. This is different from our assumption for the luminosity dependence of SEDs, namely, when the luminosity of the IR sources evolves, the SED changes with the luminosity (see § 6.3).

4. Predictions for redshift distribution of *SIRTF* sources: in Figure 24 we compare the redshift distribution of sources in the *SIRTF* 70 μm band ($f_{70\mu m} \geq 5$ mJy) predicted by R01 and by our best-fit model. While R01 predicts that most of these sources ("cirrus" and starbursts) have $z < 0.5$ (median ~ 0.4), our best-fit model predicts the opposite, namely, most sources (starbursts) have $z > 0.5$ (median ~ 1). This difference is mainly due to the different evolution rates of normal spirals ("cirrus galaxies") in the two models: in our best-fit model, the evolution rate of the normals is rather low (evolution index = 1.5). Since the normals dominate sources in the local universe, the evolution rate of overall IR sources at low z is low in our best-fit model. Only when the starbursts overtake the normals as

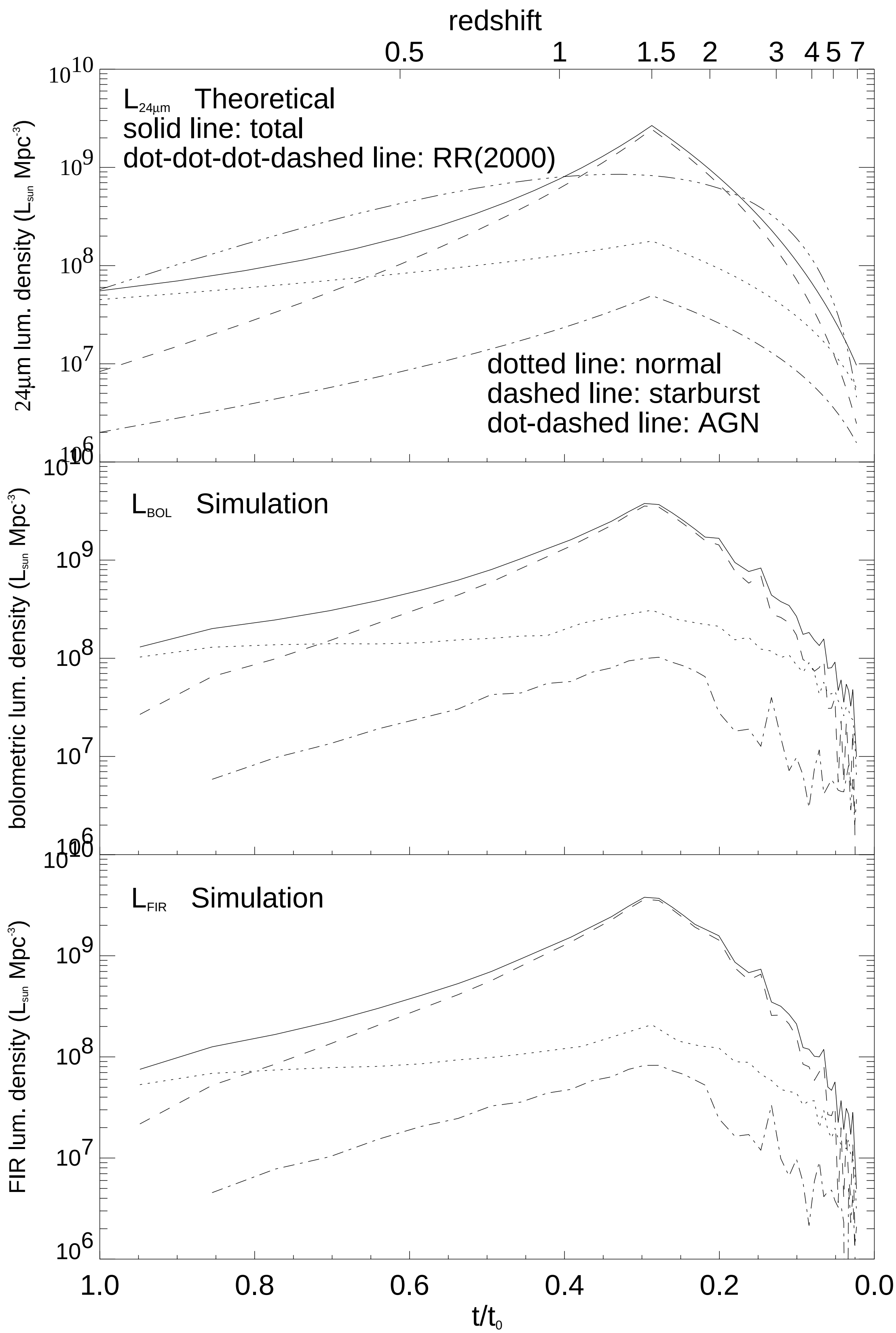

FIG. 23.—Evolution of the cosmic luminosity density, which is the sum of the luminosity of all sources in a unit comoving volume (1 Mpc^3), predicted by the best-fit model ("peak model"); t is the time since the big bang, t_0 is the current age of the universe. *Upper panel:* Luminosity density at 24 μm calculated using the evolution model. *Middle panel:* Density of bolometric luminosity (0.1–1000 μm) from a simulation ($f_{24\mu m} > 10^{-9}$ mJy, 0.01 deg^2). *Lower panel:* Density of IR luminosity (3–1000 μm) from the same simulation.

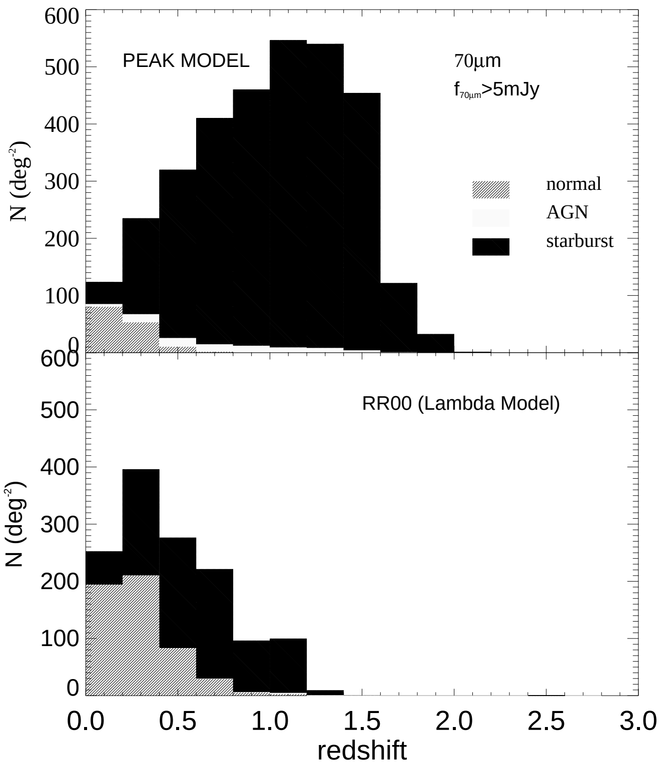

FIG. 24.—Predictions for the redshift distribution of sources in the *SIRTF* 70 μm band ($f_{70\mu m} \geq$ 5mJy): comparisons between predictions by the "peak model" of this paper and by the "Λ model" of R01.

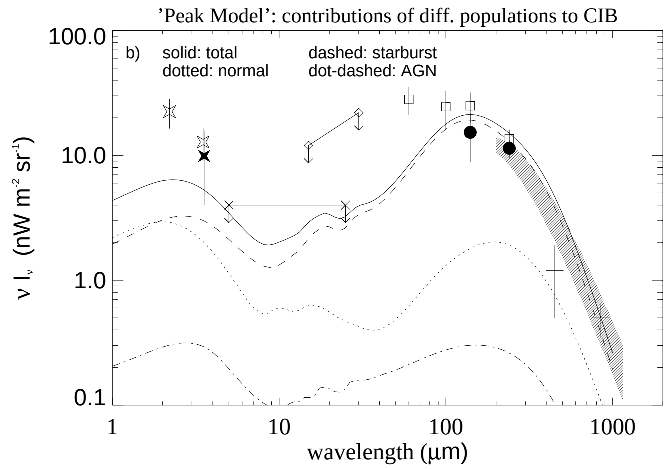

FIG. 25.—Contributions to the CIB from different populations predicted by the best-fit model ("peak model").

the dominant population, which occurs at $z \sim 0.5$, does the high evolution rate of the starbursts start to significantly affect the IR sources on the whole. On the other hand, in R01, all populations evolve with the same rate. Thus, the evolution index is ~ 3 at small redshifts for normal spirals. Consequently, as shown in the upper panel of Figure 23, the SFR (roughly proportional to the luminosity density) of R01 is about a factor of 2 higher than our best-fit model at $z < 0.5$. The SFR predicted by our best-fit model starts to catch up with R01 at higher z and then overshoots until $z \sim 1.5$. It follows that a redshift survey of *SIRTF* sources in the 70 μm band will serve as a good test to distinguish the models. It should be noted that for the sample of faint *IRAS* 60 μm sources ($f_{60\mu m} \geq 200$ mJy; Oliver et al. 1996), our best-fit model predicts too many (about a factor of 10) sources with $z > 0.4$ compared to the observations (six out of 1400; M. Rowan-Robinson 2000, private communication). However, it is not very clear to what extent the discrepancy is due to biases introduced by large-scale structures and by the incompleteness of the redshift survey (see the end of § 4). R01, which predicts about a factor of 2 less such sources than our best-fit model, gives a better fit to the redshift data.

5. CIB: the difference in the evolution rates in different populations between R01 and our best-fit model results in a significant discrepancy on the relative contributions from different populations to the counts and to the CIB. As shown in Figure 25, our model predicts that the IR to submillimeter CIB is predominantly due to the starburst galaxies. The best-fit model of R01 predicts that most of the CIB is due to "cirrus galaxies" (close to "normals" in our model), which, because they are assumed to evolve as strongly as starburst galaxies, maintain their dominance to the IR emission from the local universe throughout the high-z universe. Both of our models predict negligible contributions from AGNs to the CIB (less than 10% at any given wavelength), although the "starburst" model populations could include a significant heavily obscured segment of the AGN population that is thought to contribute significantly to the cosmic X-ray background (XRB; e.g., Gilli, Salvati, & Hasinger 2001).

6.2. *Star Formation History*

Much attention has been attracted since Madau et al. (1996) related source counts and redshift distributions obtained from deep UV/optical surveys to the star formation/metal production history of the universe. Since then the so-called Madau diagram has been revised many times through various improvements, including (1) the corrections for the effect of dust extinction on UV/optical luminosities (Madau et al. 1998; Pozzetti et al. 1998; Steidel et al. 1999), (2) results from less extinction-sensitive Balmer line surveys (Gallego et al. 1995; Tresse & Maddox 1998; Yan et al. 1999; Glazebrook et al. 1999), and (3) results from submillimeter SCUBA surveys (Barger et al. 1999).

Adopting the conversion factor of Kennicutt (1999), SFR ($M_\odot$ yr^{-1}) $= L_{\rm IR} \times 4.510^{-44}$ (ergs s^{-1}), we convert the IR (3–1000 μm) luminosity density curve plotted in Figure 23 (*lower panel*) to an SFR curve. In Figure 26 the result is compared with the survey data found in the literature. Not surprisingly, the model prediction is in very good agreement with the results from ISOCAM surveys (Flores et al. 1999) because at $z < 1.5$ the model is constrained by the ISOCAM data. On the other hand, the model prediction is slightly higher than the results of the UV/optical and Hα surveys of $z < 1.5$. After the turnover redshift, our best-fit model predicts a quick decrease, similar to what has been suggested by the UV data of Lyman break galaxies.

The "flat model," represented by the dashed line, predicts too much CIB (Fig. 9) and too many counts in the SCUBA 850 μm band (Fig. 10). The SFR of $z \gtrsim 3$ galaxies predicted by the "flat model" is about a factor of 7 higher than those derived from the UV data of Lyman break galaxies, even after the UV data are corrected for extinction (about a factor of 3; Steidel et al. 1999). Although we cannot rule out

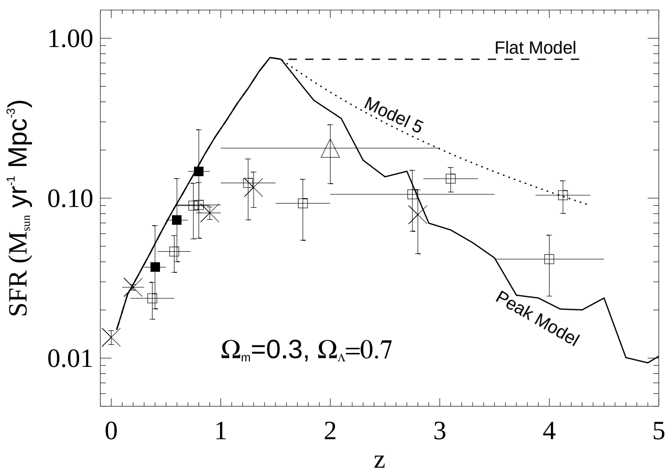

FIG. 26.—Model predictions for SFR evolution compared with observational results from the literature. *Solid line:* best-fit model ("peak model"); *dashed line:* "flat model"; *dotted line:* model 5 in Table 3; *filled squares:* SFR from ISOCAM surveys (Flores et al. 1999); *crosses:* SFR from Balmer line surveys (Gallego et al. 1995; Tresse & Maddox 1998; Yan et al. 1999; Glazebrook et al. 1999); *open squares:* SFR from UV surveys ("extinction-corrected" data taken from Fig. 9 of Steidel et al. 1999); *open triangle:* SFR from SCUBA (Barger et al. 1999). All data have been converted to the cosmology model specified by $H_0 = 75$ km s^{-1} Mpc^{-1}, $\Omega_m = 0.3$, and $\Omega_\Lambda = 0.7$.

the "flat model" because of the uncertainties associated with the evolution of the submillimeter SEDs and those associated with the extinction corrections of the UV data, it is certainly disfavored by our results. On the other hand, models between the "peak model" and the "flat model," such as the model 5 plotted by the dotted line (see also Fig. 9), are certainly allowed by our results.

6.3. *Uncertainties Introduced by Model Assumptions*

The most important assumption in this work concerns the applicability of the SED versus IR luminosity relation, found for local IR galaxies (Soifer & Neugebauer 1991; Fang et al. 1998), for high-z galaxies. Namely, we assume that the SEDs do not evolve with time for a given luminosity. Note that this is different from assuming that the SEDs of galaxies do not evolve at all because our models indeed predict strong luminosity evolution for IR galaxies and therefore, under our assumption, more galaxies in the early epochs have SEDs similar to local luminous IR galaxies, which are significantly different from the SEDs of local L_* galaxies.

This assumption is not very well constrained. Not much is known about the IR SEDs of high-z galaxies, in particular no current FIR ($\lambda \gtrsim 30$ μm) instrument is sensitive enough to detect them in the FIR bands. A few $z \gtrsim 1$ galaxies have been identified in the ISOCAM surveys (predominantly in ISOCAM 15 μm surveys; Aussel et al. 1999; Flores et al. 1999), and the optical SEDs of some of them have been obtained using *HST* images (Flores et al. 1999). The submillimeter SCUBA surveys (Hughes et al. 1998; Barger et al. 1998; Blain et al. 1999) may have detected quite a few high-z galaxies, but the positional uncertainties of the SCUBA sources are so large that it is very difficult to make cross-identifications in other bands. In fact, so far only a handful (three to five; D. T. Frayer 2000, private communication) of high-z SCUBA sources have published high-confidence optical identifications and redshifts (Ivison et al. 1998; Barger et al. 1999; Frayer et al. 1999a). The most recent results of Ivison et al. (2000) show that indeed the SEDs of these galaxies have similar shapes to local ULIRGs such as Arp 220 or Mrk 231.

High-z galaxies seen in deep surveys are high-luminosity galaxies. Thus, to the extent that they have similar SEDs to their local counterparts, our results will be valid. Namely, intrinsically faint galaxies at high z may have different SEDs than their local counterparts, but this will not have any significant effect on the predictions for number counts and the CIB. It is likely that in high-z ULIRGs the luminosities in all bands are predominantly radiated in localized starburst regions and/or AGNs, where the physical processes determining the luminosity and the SED (e.g., AGN-related processes, star formation, radiative transfer, etc.) are similar to those in local ULIRGs. In particular, both the theoretical arguments and observational evidence (Soifer et al. 1998; Armus et al. 1998) show that dust is produced rapidly after the first star formation episode in galaxies. Therefore, those high-luminosity galactic nuclei in the early universe are likely to be optically thick (Soifer et al. 1998; Armus et al. 1998), similar to their local counterparts.

It is expected that for large samples of galaxies SEDs covering 4000 Å to 160 μm will be available when *SIRTF* deep surveys and follow-up optical/NIR surveys are carried out. Then the assumption that the SED versus IR luminosity relation of local IR galaxies also holds for high-z galaxies will be fully tested.

Throughout this paper we have assumed the Λ cosmology ($\Omega_\Lambda = 0.7$, $\Omega_m = 0.3$), which is favored by recent observations of Type I supernovae in distant galaxies (Perlmutter et al. 1997; Garnavich et al. 1998). Compared to the standard $\Omega_\Lambda = 0$, $\Omega_m = 1$ Einstein–de Sitter cosmology, the comoving volume corresponding to a given z is significantly larger in the Λ cosmology (Carroll et al. 1992). Although this volume factor is partially balanced by relatively fainter flux for a given luminosity and given z in the Λ cosmology, it still affects significantly the predictions of the SCUBA counts and the submillimeter CIB, where the contribution from high-z sources is large. This is one of the reasons why a steep decrease after $z = 1.5$ is favored by our best-fit model (Fig. 26). If the Einstein–de Sitter cosmology were adopted, a flatter SFR at early epochs would have been obtained.

The assumptions for the evolution rates of normal late-type galaxies and of galaxies with AGNs (§ 3.3) are based on the results of optical and NIR surveys of these sources. Whether they also apply to the IR bands will have to be tested with future IR surveys (e.g., *SIRTF* surveys). Nevertheless, if indeed most of the evolution in IR bright galaxies is due to starburst galaxies (and possibly also highly obscured AGNs), as suggested by ISOCAM surveys (Elbaz et al. 1999; Flores et al. 1999), these uncertainties will have minimal effects on our results for the overall IR evolution.

Finally, the prominent peak at $z = 1.5$ in the SFR versus redshift plot (Fig. 25) is an artifact due to the simple two-step power-law function form adopted for the evolution functions (eqs. [7] and [8]). However, the SFR at $z < 1.5$ is mostly constrained by the ISOCAM 15 μm surveys, which indeed reach as deep as $z = 1.5$. As was argued in Paper II, a very strong evolution all the way back to $z \sim 1.5$ is needed to explain the sharp peak at $f_{15\mu m} \sim 0.4$ mJy in the Euclidean normalized differential 15 μm counts (Elbaz et al. 1999).

7. CONCLUSIONS

We have developed empirical "backward evolution" models for multiband IR surveys. A new Monte Carlo algorithm is developed for this task. It exploits a large library consisting of realistic spectral energy distributions (SEDs) of 837 local IR galaxies (*IRAS* 25 μm selected) from the UV (1000 Å) to the radio (20 cm), including *ISO*-measured 3–13 μm unidentified broad features (UIBs). The basic assumption is that the local correlation between SEDs and mid-infrared (MIR) luminosities can be applied to earlier epochs of the universe. A Λ cosmology ($\Omega_\Lambda = 0.7$, $\Omega_m = 0.3$) has been assumed throughout the paper. By attaching an SED appropriately drawn from the SED library to every source predicted by a given model, the algorithm enables simultaneous comparisons with multiple surveys in a wide range of wave bands.

IR galaxies are divided into three populations: (1) normal late-type galaxies ("normals"), (2) starburst/interacting galaxies ("starbursts"), and galaxies with AGNs ("AGNs"). Different cosmic evolution is assumed for these different populations. Parameterized (power-law) luminosity evolution functions $[F_i(z)]$ and density evolution functions $[G_i(z)]$ of the form

$$F_i(z) = \begin{cases} (1+z)^{u_i} & (z \le z_1)\,, \\ (1+z)^{v_i} & (z_1 < z \le z_0)\,, \end{cases}$$

$$G_i(z) = \begin{cases} (1+z)^{p_i} & (z \le z_1)\,, \\ (1+z)^{q_i} & (z_1 < z \le z_0) \end{cases}$$

are adopted, with $z_1 = 1.5$ and $z_0 = 7$. At $z < 1.5$, for "normals" ($i = 1$) and "AGNs" ($i = 3$) it is assumed that $u_1 = 1.5$, $p_1 = 0$ (passive luminosity evolution) and $u_3 = 3.5$, $p_3 = 0$ (evolution rate of optical QSOs), respectively. The evolution rate of "starbursts" ($i = 2$) at $z < 1.5$ is determined by fitting the ISOCAM 15 μm surveys. The best-fit results are $u_2 = 4.2$, $p_2 = 2$. At $1.5 \le z \le 7$, the evolution of IR galaxies is mostly constrained by the submillimeter counts and the CIB. It is found that a "peak model," with the p_i and u_i values described above and $v_1 = v_2 = v_3 = q_2 = -3$, gives the best fit. The "flat model," which is the same as the "peak model" at $z < 1.5$ but $v_1 = v_2 = v_3 = q_2 = 0$ at $1.5 \le z \le 7$, overpredicts significantly the SCUBA counts and the CIB.

Remarkably, the best-fit model ("peak model") gives good fits simultaneously to all data (both number counts and redshift distributions) obtained from IR surveys, including ISOCAM 15 μm, ISOPHOT 90 and 175 μm, *IRAS* 60 μm, and SCUBA 850 μm. Predictions for contributions of IR bright sources to counts in other wave bands, such as the optical *B* band, the NIR *K* band, and the radio continuum 20 cm band, are also in agreement with the literature. This suggests that the model is robust.

Predictions for number counts, confusion limits, redshift distributions, and color-color diagrams are made for multiband surveys using the upcoming *SIRTF* satellite. It is found that several *SIRTF* colors can be useful indicators of galaxy populations and redshifts.

Glenn Morrison is acknowledged for help in collecting the VLA data. George Rieke is thanked for pointing out a computational error in a previous version of this paper. Helpful comments from Andrew Blain, George Helou, Rob Ivison, Tom Soifer, and an anonymous referee are acknowledged. This research has made use of the NASA/IPAC Extragalactic Database (NED), which is operated by the Jet Propulsion Laboratory, California Institute of Technology, under contract with the National Aeronautics and Space Administration. This work has made use of data products from the Two Micron All Sky Survey (2MASS), which is a joint project of the University of Massachusetts and the Infrared Processing and Analysis Center/California Institute of Technology, funded by the National Aeronautics and Space Administration and the National Science Foundation. This work has made use of data services of the Infrared Science Archive (IRSA) at the Infrared Processing and Analysis Center/California Institute of Technology, funded by the National Aeronautics and Space Administration. This work has also made use of data products from the NRAO VLA Sky Survey (NVSS) and the Faint Images of the Radio Sky at Twenty cm (FIRST), both of which are NRAO projects carried out using the NRAO Very Large Array (VLA). The authors were supported by the Jet Propulsion Laboratory, California Institute of Technology, under contract with NASA.

APPENDIX

CORRELATIONS BETWEEN FLUX DENSITIES IN THE FIR AND SUBMILLIMETER BANDS

In this appendix, empirical correlations between flux densities in the *IRAS* 60 and 100 μm bands and in the submillimeter bands at 170, 240, 450, 850, and 1200 μm are studied. The results have been applied to the SED model in order to extend the SEDs to the submillimeter (up to 1200 μm) wave bands (§ 2).

Flux densities in the submillimeter wave bands were collected from the literature. In the 170 μm band (including all data between the 160 and 180 μm bands), data for 29 galaxies were found in Devereux & Young (1992), Engargiola (1991), Klaas et al. (1997), Hippelein et al. (1996), and Stickel et al. (1998). In the 240 μm band, flux densities were found for 20 galaxies (including 14 upper limits) in Odenwald, Newmark, & Smoot (1998). In the 450 μm band, 16 detections and seven upper limits were found in Rigopoulou et al. (1996), Frayer et al. (1999b), Eales, Wynn-Williams, & Duncan (1989), Dunne et al. (2000), and Alton et al. (1998). In the 850 μm band (including also the 800 μm band), 121 flux densities (including one upper limit) were found in Lisenfeld et al. (2000), Dunne et al. (2000), Alton et al. (1998), Rigopoulou et al. (1996), Hughes, Gear, & Robson (1990), Frayer et al. (1999b), and Eales et al. (1989). In the 1200 μm band (including all observations between the 1000 and 1300 μm bands), 62 detections and four upper limits were found in Andreani & Franceschini (1996), Rigopoulou et al. (1996), Hughes et al. (1990), Eales et al. (1989), Chini et al. (1986), and Fich & Hodge (1993). Color-color diagrams of $\log\,(f_{\mathrm{submm},i}/f_{100\mu\mathrm{m}})$ versus $\log\,(f_{100\mu\mathrm{m}}/f_{60\mu\mathrm{m}})$, where $f_{\mathrm{submm},i}$ is one of the submillimeter flux densities listed above, are plotted in Figures 27–32. In Figures 31 and 32, color-color diagrams of $\log\,(f_{1200\mu\mathrm{m}}/f_{100\mu\mathrm{m}})$ versus $\log\,(f_{100\mu\mathrm{m}}/f_{60\mu\mathrm{m}})$ are plotted for

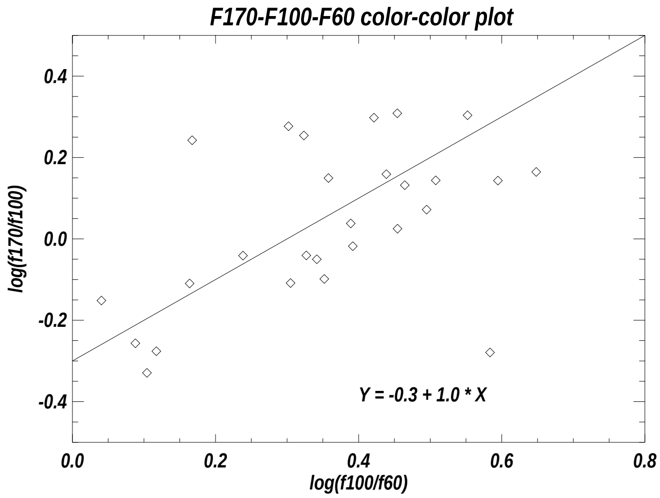

FIG. 27.—Color-color diagram of log $(f_{170\mu m}/f_{100\mu m})$ vs. log $(f_{100\mu m}/f_{60\mu m})$

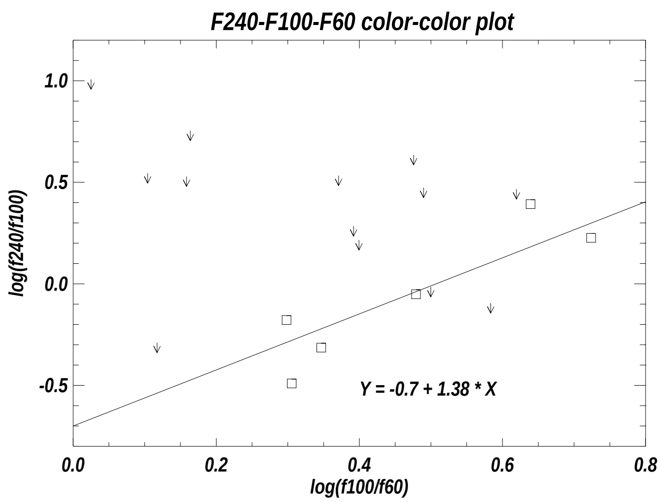

FIG. 28.—Color-color diagram of log $(f_{240\mu m}/f_{100\mu m})$ vs. log $(f_{100\mu m}/f_{60\mu m})$

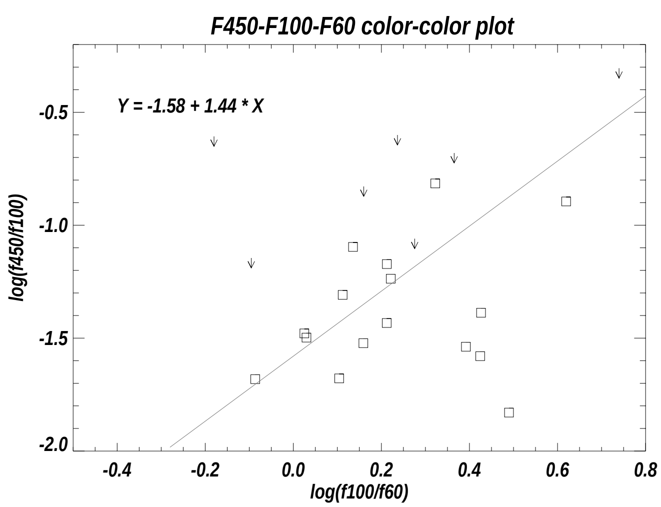

FIG. 29.—Color-color diagram of log $(f_{450\mu m}/f_{100\mu m})$ vs. log $(f_{100\mu m}/f_{60\mu m})$

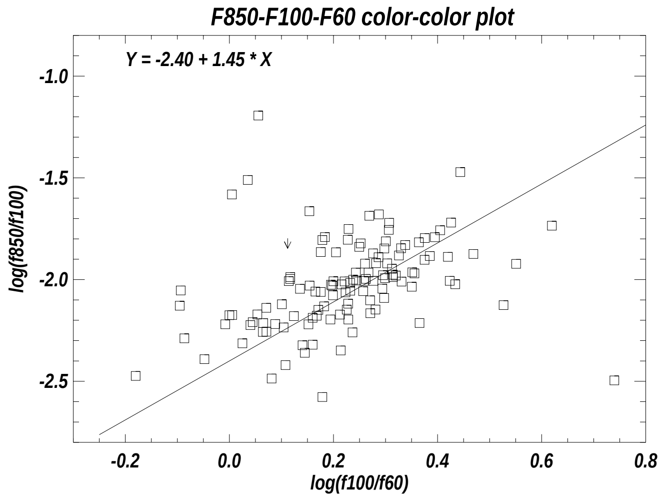

FIG. 30.—Color-color diagram of log ($f_{850\mu m}/f_{100\mu m}$) vs. log ($f_{100\mu m}/f_{60\mu m}$)

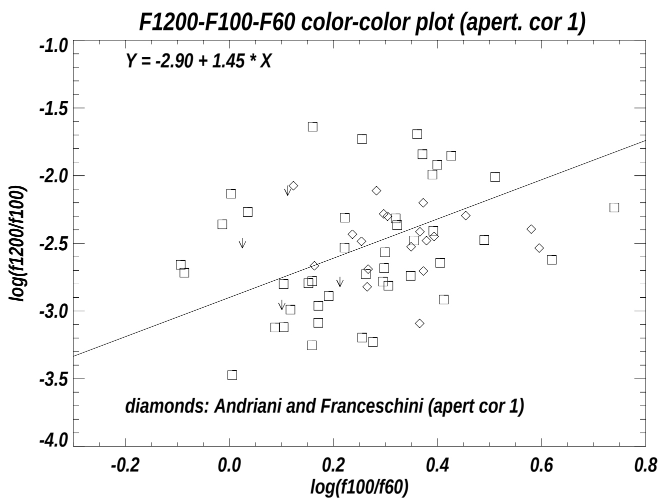

FIG. 31.—Color-color diagram of log ($f_{1200\mu m}/f_{100\mu m}$) vs. log ($f_{100\mu m}/f_{60\mu m}$). Sources (19) in Andreani & Franceschini (1996) are aperture corrected using method 1 of Andreani & Franceschini (1996).

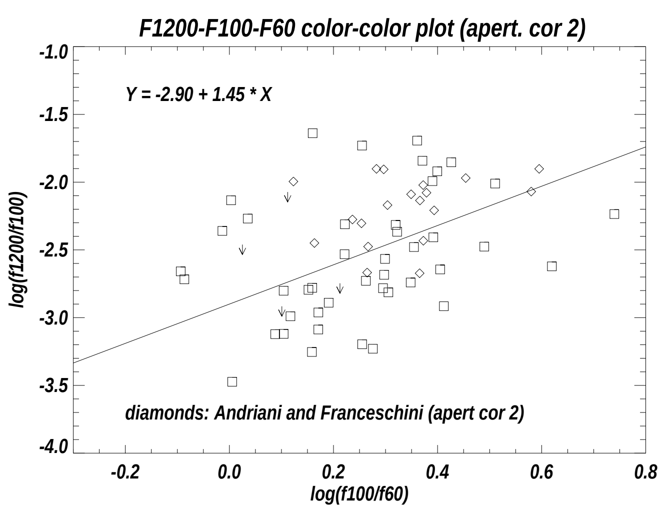

FIG. 32.—Color-color diagram of log ($f_{1200\mu m}/f_{100\mu m}$) vs. log ($f_{100\mu m}/f_{60\mu m}$). Sources (19) in Andreani & Franceschini (1996) are aperture corrected using method 2 of Andreani & Franceschini (1996).

TABLE A1

PARAMETERS OF log ($f_{\mathrm{submm},i}/f_{100\mu\mathrm{m}}$) VERSUS log ($f_{100\mu\mathrm{m}}/f_{60\mu\mathrm{m}}$) RELATION

Wave Band (μm)	Detections	Upper Limits	A_i	B_i	Figure
170	29	...	−0.3	1.0	27
240	6	14	−0.7	1.36	28
450	16	7	−1.58	1.44	29
850	121	1	−2.40	1.45	30
1200	62	4	−2.90	1.45	31 and 32

the same sources, with the sources in the list of Andreani & Franceschini (1996) (19 sources) being aperture corrected in two different ways as given in Andreani & Franceschini (1996), respectively. Linear relations in the form of

$$\log\left(\frac{f_{\mathrm{submm},i}}{f_{100\ \mu\mathrm{m}}}\right) = A_i + B_i \log\left(\frac{f_{100\ \mu\mathrm{m}}}{f_{60\ \mu\mathrm{m}}}\right) \tag{A1}$$

were derived (eyeball) from these color-color diagrams. In Table A1, the resulting A_i and B_i are listed. For a given source (with detected *IRAS* flux densities $f_{60\ \mu\mathrm{m}}$ and $f_{100\ \mu\mathrm{m}}$) in the SED sample, the submillimeter flux density in any of the given bands is then estimated using the relation

$$\log(f_{\mathrm{submm},i}) = \log(f_{100\ \mu\mathrm{m}}) + A_i + B_i \log\left(\frac{f_{100\ \mu\mathrm{m}}}{f_{60\ \mu\mathrm{m}}}\right). \tag{A2}$$

It should be noted that the correlations plotted in the FIR/submillimeter color-color diagrams are generally rather poor. There are often only a small number of sources in a plot, and many of them are upper limits. The data are also very heterogeneous, obtained from observations with widely different apertures. Aperture corrections were included only when available in the literature. When there is more than one observation for a given source in a given band, the data from the observation with the largest aperture are taken. Consequently, the lines in the color-color plots that represent our best (eyeball) estimates of the log ($f_{\mathrm{submm},i}/f_{100\mu\mathrm{m}}$) versus log ($f_{100\mu\mathrm{m}}/f_{60\mu\mathrm{m}}$) relations are very uncertain. This reflects the true situation in the current literature of extragalactic submillimeter sources. Nevertheless, it appears that the submillimeter SEDs derived using flux densities predicted by these relations agree well with the observations for a wide variety of extragalactic sources (Fig. 2), and the good agreement between the simulated and measured 850 μm and 1.2 mm LFs (Figs. 5 and 6) further supports the validity of these empirical relations. We have deliberately avoided any modeling in deriving the relations, keeping them purely empirical. They will set constraints to theoretical models of dust heating in galaxies (e.g., Silva et al. 1998; Dale et al. 2001; Popescu et al. 2000).

REFERENCES

Adelberger, K. L., & Steidel, C. C. 2000, ApJ, 544, 218
Alton, P. B., Bianchi, S., Rand, R. J., Xilouris, E. M., Davies, J. I., & Trewhella, M. 1998, ApJ, 507, L125
Andreani, P., & Franceschini, A. 1996, MNRAS, 283, 85
Armus, L., Matthews, K., Neugebauer, G., & Soifer, B. T. 1998, ApJ, 506, L89
Aussel, H., Cesarsky, C. J., Elbaz, D., & Starck, J. L. 1999, A&A, 342, 313
Barger, A. J., et al. 1998, Nature, 394, 248
———. 1999, ApJ, 518, L5
Becker, R. H., White, R. L., & Helfand, D. J. 1995, ApJ, 450, 559
Benford, D. 1999, Ph.D. thesis, Caltech
Bershady, M. A., Lowenthal, J. D., & Koo, D. C. 1998, ApJ, 505, 50
Bertin, E., Dennefeld, M., & Moshir, M. 1997, A&A, 323, 685
Bicay, M. D., Beichman, C. A., Cutri, R. M., & Madore, B. F. 1999, ASP Conf. Ser. 177, Astrophysics with Infrared Surveys: A Prelude to *SIRTF* (San Francisco: ASP)
Blain, A. W., Smail, I., Ivison, R. J., & Kneib, J.-P. 1999, MNRAS, 302, 632
———. 2000, in ASP Conf. Ser. 193, The Hy-Redshift Universe: Galaxy Formation and Evolution at High Redshift, ed. A. J. Bunker & W. J. M. van Breughel (San Francisco: ASP), 246
Boyle, B. J., Shank, T., & Peterson, B. A. 1988, MNRAS, 235, 935
Carico, D. P., Keene, J., Soifer, B. T., & Neugebauer, G. 1992, PASP, 104, 1086
Carlberg, R. G., Pritchet, C. J., & Infante, L. 1994, ApJ, 435, 540
Carroll, S. M., Press, W., & Turner, E. 1992, ARA&A, 30, 499
Chini, R., Kruegel, E., & Kreysa, E. 1986, A&A, 166, L8
Ciliegi, P., et al. 1999, MNRAS, 302, 222
Clavel, J., et al. 2000, A&A, 357, 839
Clements, D. L., Desert, F.-X., Franceschini, A., Reach, W. T., Baker, A. C., Davies, J. K., & Cesarsky, C. 1999, A&A, 346, 383
Condon, J. J. 1984, ApJ, 284, 44
Condon, J. J., et al. 1998, AJ, 115, 1693
Condon, J. J., Helou, G., Sanders, D. B., & Soifer, B. T. 1990, ApJS, 73, 359
Connolly, A. J., Szalay, A. S., Dickinson, M., SubbaRao, M. U., & Brunner, R. J. 1997, ApJ, 486, L11
Dale, D. A., Helou, G., Contursi, A., Silbermann, N. A., & Sonali, K. 2001, ApJ, 549, 215
de Grijp, M. H. K., Miley, K. K., Lub, J., & de Jong, T. 1985, Nature, 314, 240
Devereux, N. A., & Young, J. S. 1992, AJ, 103, 1536
Dole, H., et al. 2000, in ISO beyond Point Sources: Studies of Extended Infrared Emission, ed. R. J. Laureijs, K. Leach, & M. F. Kessler (Noordwijk: ESA), 167
———. 2001, A&A, 372, 364
Driver, S. P., et al. 1995, ApJ, 449, L23
Dunne, L., Eales, S., Edmunds, M., Ivison, R., Alexander, P., & Clements, D. L. 2000, MNRAS, 315, 115
Dwek, E., & Arendt, R. G. 1998, ApJ, 508, L9
Dwek, E., et al. 1998, ApJ, 508, 106
Dwek, E., & Slavin, J. 1994, ApJ, 436, 696
Eales, S. A., Wynn-Williams, C. G., & Duncan, W. D. 1989, ApJ, 339, 859
Efstathiou, A., et al. 2000a, MNRAS, 319, 1169
Efstathiou, A., Rowan-Robinson, & Siebenmorgen, R. 2000b, MNRAS, 313, 734
Elbaz, D., et al. 1998a, in 34th Liege Astrophysics Colloq., The Next Generation Space Telescope: Science Drivers and Technological Challenges, ed. B. Kaldeich-Schurmann (Noordwijk: ESA), 47
———. 1998b, in The Universe as Seen by *ISO*, ed. P. Cox & M. F. Kessler (Noordwijk: ESA), 999
———. 1999, A&A, 351, L37
Engargiola, G. 1991, ApJS, 76, 875
Fang, F., Shupe, D. L., Xu, C., & Hacking, P. B. 1998, ApJ, 500, 693
Fich, M., & Hodge, P. 1993, ApJ, 415, 75
Finkbeiner, D. P., Davis, M., & Schlegel, D. J. 2000, ApJ, 544, 81
Fixsen, D. J., Dwek, E., Mather, J. C., Bennett, C. L., & Shafer, R. A. 1998, ApJ, 508, 123

Flores, H., et al. 1999, ApJ, 517, 148
Franceschini, A., Andreani, P., & Danese, G. 1998, MNRAS, 296, 709
Franceschini, A., Danese, L., De Zotti, G., & Xu, C. 1988, MNRAS, 233, 175
Frayer, D. T., et al. 1999a, ApJ, 514, L13
Frayer, D. T., Ivison, R. J., Smail, I., Yun, M. S., & Armus, L. 1999b, AJ, 118, 139
Gallego, J., Zamorano, J., Aragon-Salamanca, A., & Rego, M. 1995, ApJ, 455, L1
Gardner, J. P., Sharples, R. M., Carrasco, B. E., & Frenk, C. S. 1996, MNRAS, 282, L1
———. 1997, ApJ, 480, L99
Garnavich, P. M., et al. 1998, ApJ, 509, 74
Gautier, T. N., III, Boulanger, F., Perault, M., & Puget, J. L. 1992, AJ, 103, 1313
Gilli, R., Salvati, M., & Hasinger, G. 2001, A&A, 366, 407
Glazebrook, K., Blake, C., Economou, F., Lilly, S., & Colless, M. 1999, MNRAS, 306, 843
Glazebrook, K., Ellis, R., Santiago, B., & Griffiths, R. 1995, MNRAS, 275, L19
Gorjian, V., Wright, E. L., & Chary, R. R. 2000, ApJ, 536, 550
Gregorich, D. T., Neugebauer, G., Soifer, B. T., Gunn, J. E., & Herter, T. L. 1995, AJ, 110, 259
Hacking, P. B., Condon, J. J., & Houck, J. R. 1987, ApJ, 316, L15
Hacking, P. B., & Houck, J. R. 1987, ApJS, 63, 311
Hacking, P. B., & Soifer, B. T. 1991, ApJ, 367, L49
Hauser, M. G., et al. 1998, ApJ, 508, 25
Helou, G. 1986, ApJ, 311, L33
Helou, G., & Beichman, C. A. 1990, in Proc. 29th Liège International Astrophysical Colloq., From Ground-based to Space-borne Submillimeter Astronomy (ESA SP-314; Noordwijk: ESA), 117
Helou, G., Lu, N. Y., Werner, M. W., Malhotra, S., & Silbermann, N. 2000, ApJ, 532, L21
Hippelein, H., et al. 1996, A&A, 315, L79
Huang, J.-S., Cowie, L., & Luppino, G. 1998, ApJ, 496, 31
Hughes, D. H., et al. 1998, Nature, 394, 241
Hughes, D. H., Gear, W. K., & Robson, E. I. 1990, MNRAS, 244, 759
Infante, L., de Mello, Du. F., & Menanteau, F. 1996, ApJ, 469, L85
Ivison, R., et al. 1998, MNRAS, 298, 583
———. 2000, MNRAS, 315, 209
Kawara, K., et al. 1998, A&A, 336, L9
Kennicutt, R. C., Jr. 1999, ApJ, 525C, 1165
Kessler, M. F., et al. 1996, A&A, 315, L27
Klaas, U., Haas, M., Heinrichsen, I., & Schulz, B. 1997, A&A, 325, L21
La Franca, F., et al. 2000, Mem. Soc. Astron. Italiana, in press (astro-ph/0006177)
Lagache, G., Albergel, A., Boulanger, F., & Puget, J.-L. 1998, A&A, 333, 709
Le Févre, O., et al. 2000, MNRAS, 311, 565
Lilly, S. J., Le Févre, O., Hammer, F., & Crampton, D. 1996, ApJ, 460, L1
Lisenfeld, U., Isaak, K. G., & Hills, R. 2000, MNRAS, 312, 433
Lonsdale, C. J. 2000, in ASP Conf. Ser. 177, Astrophysics with Infrared Surveys: A Prelude to *SIRTF*, ed. M. D. Bicay, C. A. Beichman, R. M. Cutri, & B. F. Madore (San Francisco: ASP), 24
Lonsdale, C. J., & Hacking, P. B. 1989, ApJ, 339, 712
Lonsdale, C. J., Hacking, P. B., Conrow, T. B., & Rowan-Robinson, M. 1990, ApJ, 358, 60
Madau, P., et al. 1996, MNRAS, 283, 1388
Madau, P., Pozzetti, L., & Dickinson, M. 1998, ApJ, 498, 106
Metcalfe, N., Shanks, T., Fong, R., & Jones, L. R. 1991, MNRAS, 249, 498
Metcalfe, N., Shanks, T., Fong, R., & Roche, N. 1995, MNRAS, 273, 257
Minezaki, T., Kobayashi, Y., Yoshii, Y., & Peterson, B. A. 1998, ApJ, 494, 111
Niklas, S., Klein, U., Braine, J., & Wielebinski, R. 1995, A&AS, 114, 21
Niklas, S., Klein, U., & Wielebinski, R. 1997, A&A, 322, 19
Odenwald, S., Newmark, J., & Smoot, G. 1998, ApJ, 500, 554
Oliver, S. J., et al. 1996, MNRAS, 280, 673
———. 2000, MNRAS, 316, 749
Pearson, C., & Rowan-Robinson, M. 1996, MNRAS, 283, 174
Pei, Y. C. 1995, ApJ, 438, 623
Perlmutter, S., et al. 1997, ApJ, 483, 565
Popescu, C. C., Misiriotis, A., Kylafis, N. D., Tuffs, R. J., & Fischera, J. 2000, A&A, 362, 138
Pozzetti, L., Madau, P., Zamorani, G., Ferguson, H. C., & Bruzual, G. 1998, MNRAS, 298, 1133
Puget, J.-L., et al. 1996, A&A, 308, L5
———. 1999, A&A, 345, 29
Puget, J. L., & Léger, A. 1989, ARA&A, 27, 161
Richards, E. A., Fomalont, E. B., Kellermann, K. I., Windhorst, R. A., Partridge, R. B., Cowie, L. L., & Barger, A. J. 1999, ApJ, 526, L73
Rigopoulou, D., Lawrence, A., & Rowan-Robinson, M. 1996, MNRAS, 278, 1049
Roche, N., & Eales, S. A. 1999, MNRAS, 307, 111
Roche, P. F., & Chandler, C. J. 1993, MNRAS, 265, 486
Rowan-Robinson, M. 2001, ApJ, 549, 745 (R01)
Rowan-Robinson, M., et al. 1997, MNRAS, 289, 490
Rowan-Robinson, M., Hughes, J., Vedi, K., & Walker, D. W. 1990, MNRAS, 246, 273
Sanders, D. B., & Mirabel, I. F. 1996, ARA&A, 34, 749
Saunders, W., et al. 1990, MNRAS, 242, 318
Serjeant, S., et al. 2000, MNRAS, 316, 768
Shupe, D. L., Fan, F., Hacking, P. B., & Huchra, J. P. 1998, ApJ, 501, 597
Silva, L., Granato, G. L., Bressan, A., & Danese, L. 1998, ApJ, 509, 103
Simpson, C., & Eisenhardt, P. 1999, PASP, 111, 691
Soifer, B. T., et al. 1994, ApJ, 420, L1
Soifer, B. T., & Neugebauer, G. 1991, AJ, 101, 354
Soifer, B. T., Neugebauer, G., Franx, M., Matthews, K., & Illingworth, G. D. 1998, ApJ, 501, L171
Spinoglio, L., Malkan, M. A., Rush, B., Carrasco, L., & Recillas-Cruz, E. 1995, ApJ, 453, 616
Spoon, H. W. W., Koornneef, J., Moorwood, A. F. M., Lutz, D., & Tielens, A. G. G. M. 2000, A&A, 357, 898
Stanev, T., & Franceschini, A. 1998, ApJ, 494, L159
Steidel, C. C., Adelberger, K., Giavalisco, M., Dickinson, M., & Pettini, M. 1999, ApJ, 519, 1
Stickel, M., et al. 1998, A&A, 336, 116
Trentham, N., Blain, A. W., & Goldader, J. 1999, MNRAS, 305, 61
Tresse, L., & Maddox, S. J. 1998, ApJ, 495, 691
Williams, R. E., et al. 1996, AJ, 112, 1335
Xu, C. 2000, ApJ, 541, 134 (Paper II)
Xu, C., Hacking, P. B., Fan, F., Shupe, D. L., Lonsdale, C. J., Lu, N. Y., & Helou, G. X. 1998, ApJ, 508, 576 (Paper I)
Yahil, A., Strauss, M., Davis, M., & Huchra, J. P. 1991, ApJ, 372, 380
Yan, L., McCarthy, P. J., Freudling, W., Teplitz, H. I., Malumuth, E. M., Weymann, J., & Malkan, M. A. 1999, ApJ, 519, L47
Yoshii, Y., & Takahara, F. 1988, ApJ, 326, 1